Progress in Oceanography 211 (2023) 102968

Contents lists available at ScienceDirect

Progress in Oceanography

journal homepage: www.elsevier.com/locate/pocean

Review

Diapycnal mixing in the Brazil-Malvinas confluence front

Elena Roget [a,*], Josep L. Pelegrí [b], Jesús Planella-Morato [a,c], Joan Puigdefàbregas [b], Mikhail Emelianov [b], Ignasi Vallès-Casanova [b], Dorleta Orúe-Echevarria [b]

[a] Department de Física, Universitat de Girona, Girona, Spain
[b] Department d'Oceanografia Física i Tecnològica, Institut de Ciencias del Mar, CSIC, Barcelona, Spain
[c] University School of Health and Sport (EUSES), Universitat de Girona, Girona, Spain

A B S T R A C T

Diapycnal mixing in the Brazil-Malvinas Confluence Zone (BMC) is assessed on the basis of microstructure measurements done as part of an April 2017 cruise, which explored the mesoscalar and regional frontal dynamics. Sampling was done down to 400 m in 11 locations on both sides of the BMC, over the slope and in the abyssal waters. Turbulent scales, non-dimensional numbers, energy dissipation rates and diapycnal eddy diffusivities are calculated, which allow us to assess the state of the small-scale turbulence in the frontal region.

Active turbulence was present at all depths and stations, with high-dissipation patches ranging from several metres to a few tens of metres. The frontal zone is characterized by high energy dissipation and eddy diffusivity. The geometric mean eddy diffusivity for all stations and the entire water column is 7.0×10^{-4} m^2 s^{-1}. The mean values halve when only considering the more stratified seasonal thermocline, 3.8×10^{-4} m^2 s^{-1}, and are twice larger south than north of the BMC.

High dissipation rates coincide with high vertical shear, possibly related to the convergence of the two intense currents and/or the generation of internal waves by the associated mesoscalar and submesoscalar features. The layered structures related to intruding filaments favor double diffusive convection and salt fingering. Near-bottom mixing at the stations on the continental slope is possible related to shear-driven Kelvin-Helmoltz instabilities.

1. Introduction

Diapycnal mixing (across isopycnal surfaces) plays a crucial role in the exchange of waters between the oceanic thermocline, which are directly ventilated by the wind pumping, and the isolated deep abyssal layers. In particular, diapycnal mixing is the main driver that turns the abyssal dense waters into lighter overlying waters along the meridional overturning pathway (Munk, 1966; Wunsch and Ferrari, 2004), with upper-ocean mixing having a high effect on poleward heat transport (Gregg et al., 2018). Vertical mixing also has a crucial role in the biogeochemical cycles, being the principal process behind nutrient fluxes that sustain primary production in the photic layers (Gnanadesikan et al., 2002; Pelegrí et al., 2006; Pollard et al., 2006; Mahadevan, 2016).

There is a general consensus that the global averaged diapycnal eddy diffusivity of mass (diapycnal mixing rates) below 1000 m is K_ρ 10^{-4} m^2 s^{-1} and in the thermocline of the open ocean K_ρ 10^{-5} m^2 s^{-1} (St. Laurent and Simmons, 2006). Nevertheless, we have learnt to recognize that the diapycnal eddy diffusivity presents high spatial and temporal variability as a response to different processes (Meyer et al., 2015; Mackinnon et al., 2017). Sources of mixing in the upper ocean include surface waves and inertial motions (Philips and Banner, 1974; Alford, 2001; Sullivan et al., 2014; Waterhouse et al., 2014), wind stress and surface fluxes (Price et al., 1986; Jing and Wu, 2010), internal waves (Egbert and Ray, 2000; Matsuno et al., 2005) and topographic and bottom-induced turbulence (Inall et al., 2021, Bastida et al., 2012; Stevens, 2018).

Frontal systems are sites of intense mean and eddy kinetic energy, characterized by numerous *meso-* and sub-mesoscale features that result from different types of instabilities as well as by along-isopycnal subduction that leads to interleaving thermohaline structures (Matsuno et al., 2005; Han et al., 2011; Johnston et al., 2011; D'Asaro et al., 2011). Caulfield (2021) recently highlighted our emerging understanding of the importance of layering in the energy cascade towards dissipative turbulence. Different mechanisms have been proposed as leading to step-like structures in stratified shear flows (Philips, 1972; Pelegrí and Sangrà, 1998; Taylor and Zhou, 2017).

At the smallest scales, turbulent kinetic energy is generated by shear-induced gravitational instability (Geyer et al., 2010) and the breaking of internal waves, and the subsequent collapse of Kelvin–Helmholtz billows (Mahony, 1977; Smyth and Moum, 2012) or Holmboe instabilities (Wunsh and Keller, 2013). Shear instabilities caused by nongeostrophic shear have been identified in fronts as a source of dissipating turbulence (Nagai, et al., 2012; Carpenter et al., 2020). Double diffusive convection is now accepted as a relevant mechanism driving mixing and turbulent

* Corresponding author.
E-mail address: elena.roget@udg.edu (E. Roget).

https://doi.org/10.1016/j.pocean.2023.102968
Received 20 July 2022; Received in revised form 10 December 2022; Accepted 10 January 2023
Available online 21 January 2023

dissipation at the smallest scales (Mack, 1985; Hamilton et al., 1989; Sanchez and Roget, 2007), with salt fingers as a primary source for diapycnal mixing (St. Laurent and Schmitt, 1999; Arcos-Pulido et al., 2014; Ferron et al., 2021).

Thomas et al. (2016) and Wenegrat et al. (2020) have concluded that mixing across the Gulf Stream front exceeds what could be attributed to atmospheric forcing. Nagai et al. (2012) found in the Kuroshio front values of eddy kinetic energy dissipation between one and two orders of magnitude larger than expected by the law of the wall. Recently, in the frontal system formed by the encounter of the Brazil and Malvinas Currents (BC and MC) – the Brazil-Malvinas Confluence (BMC) – Gunn et al. (2021) also reported very high turbulent dissipation rates and mass diffusivities based on indirect seismic oceanography data. Koenig et al. (2020) studied the upper 100 m at the Artic Front and found that the turbulence structure was consistent with heat and momentum fluxes at the surface.

An improved forecast of ocean circulation depends critically on our improved understanding of the different dynamic mechanisms that operate at different scales and lead to irreversible mixing (Canuto and Cheng, 2020), which connects to the necessity of resolving the energy pathways in geophysical dynamics (Caulfield, 2021). However, there is yet a major gap in the knowledge of those small-scale instabilities that set the turbulence parameters and determine mixing efficiency. Many more small-scale field observations are still needed to complement the laboratory and numerical studies (Gregg et al., 2018).

The Brazil Current is the western boundary current of the South Atlantic subtropical gyre and the Malvinas Current is a branch of the Antarctic Circumpolar Current flowing northward along the South Atlantic slope. At the BMC, the BC separates from the slope and retroflects northward while the Malvinas Current is subducted and partly deflected to the southeast (Gordon, 1989). Both retroflections generate eddies with horizontal scale of tens of kilometres and vertical scale up to a few hundreds of metres (Legeckis and Gordon, 1982; Lentini et al., 2006; Orúe-Echevarría, et al., 2019a, 2021). The BMC zone is one of the strongest and deepest frontal regions in the world's oceans (Orsi et al.,1999; Stramma and England, 1999) where there are exchanges between the warm (>10 °C) and salty (>35 ppt) South Atlantic Central Waters and the cold (<7 °C), fresh (<34.3 ppt) and oxygenated sub-Antarctic masses (Jullion et al., 2010; Orúe-Echevarría et al., 2019a, 2021), as well as between the shelf and deep ocean waters. The frontal region reaches down almost to the sea floor and the sea surface temperature (SST) gradient can be as high as 1 °C km^{-1} (Stramma et al., 2004). The spatial variability in the region is very high, at all regional (Paniagua et al., 2018; Goni et al., 2011), mesoscalar (Orúe-Echevarría et al., 2019a, 2021) and submesoscalar (Orúe-Echevarría et al., 2019b) scales.

Here we present first microstructure measurements in the BMC region, carried out in April 2017 down to 400 m, with the objective of providing the mean values and spatial variability of the dissipations rates and mass diapycnal diffusivities. These results are then related to the dynamics of the region, exploring the different small-scale processes that may be leading to diapycnal mixing. In section 2 the field cruise is described, presenting the site, the meteorological, the hydrographic, velocity and microstructure measurements as well as the basic processing of data. In section 3 the methodological procedures are described, including the different variables that characterize stratification, the turbulent scales, the dissipation rates, and the ratios between the different small-scale forcing mechanisms that may play a role in the development of dissipative turbulence. In section 4 we characterize the observation site at the time of measurements: the water masses (4.1), the mean flow characteristics (4.2) and the vertical structure of the water column (4.3). The results regarding the turbulence are presented in sections 5 and 6, with a brief discussion within each subsection. Section 5 focuses on the turbulent kinetic energy dissipation: the dissipation rates at different stations (5.1) and how these values compare with standard parametrization using the surface momentum and heat fluxes (5.2); this is followed by an analysis of the presence of turbulent patches in the permanent thermocline (5.3) and the overall state of the turbulence (5.4). Section 6 looks at the diapycnal eddy diffusivities: the mean values (6.1), the differences between different areas (6.2), and the driving mechanisms at the dissipative scales (6.3). We close with the main conclusions in section 7.

Table 1
Location, date and total depth of those stations where microstructure data were recorded. The microstructure casts performed at each station are also indicated.

Station	Date / Day (2017)	Location	Depth (m)	Microstructure casts
03	13 April / 103	41 12.67 S / 56 48.28 W	1090	*P3* to P5
06	14 April / 104	39 53.00 S / 54 28.71 W	3150	P8 to P11
09	15 April / 105	38 58.20 S / 53 54.61 W	3294	P15 to P18
10	15 April / 105	38 49.38 S / 54 17.49 W	1190	P19
19	16 April / 106	39 36.04 S / 55 45.34 W	428	P20 to *P23*
21	16 April / 106	39 52.64 S / 54 55.29 W	547	P25 to P27
22	19 April / 109	40 36.07 S / 54 54.82 W	3305	P28 to P30
23	19 April / 109	40 19.50 S / 55 15:68 W	1688	*P31* and *P32*
24	19 April / 109	40 05.55 S / 55 35:53 W	1200	P33 to P34
26	22 April / 112	40 16.08 S / 55 27.42 W	1450	P35 to P39
32	24 April / 114	37 00.07 S / 53 00.14 W	2900	P40 and *P41*

2. Measurements and basic processing

2.1. Site

Microstructure measurements were recorded as part of the rETRO-BMC cruise (from April 8th to 28th, 2017). A full description of the cruise and methods is provided in Orúe-Echevarría et al. (2020) and the datasets are available at Pelegrí et al. (2019). In particular, the cruise provided a comprehensive three-dimensional (view of the frontal system, with 33 hydrographic stations down to the seafloor (or at least 2000 m) and about 1371-km of sampling with an instrumented undulating vehicle (SeaSoar) -spatial resolution of about 4 × 9 km between 5 and 360 m depths-, in all cases leading to data with 1-m vertical resolution. The microstructure profiles or casts were recorded down to a maximum depth of 400 m at 11 hydrographic stations between 13 and 24 of April (Table 1). These stations covered different regions of the BMC: station 32, upstream at the Brazil Current; stations 06, 09 and 10, north of the front; stations 22, 23, 24 and 26, south of the front; stations 19 and 21, over the continental slope; and station 03, along the Malvinas Current (Fig. 1).

Notice that we position the BMC by its surface expression, although the frontal system is tilted northwards, so that those stations on the northern side actually sample the subsurface frontal structure (Fig. 2). In the frontal region, the vertical thermal structures vary largely between stations and well-defined interleaving thermal structures are often observed presenting a complex field of thermohaline intrusions between the subtropical and subantarctic water masses.

2.2. Meteorological measurements

During the campaign, standard meteorological data were recorded every hour at a height of 15.35 m from instruments on the ship's mast, and with an anemometer placed at a height of 27.50 m. The near sea-surface (about 5 m depth) temperature was also recorded in a near-

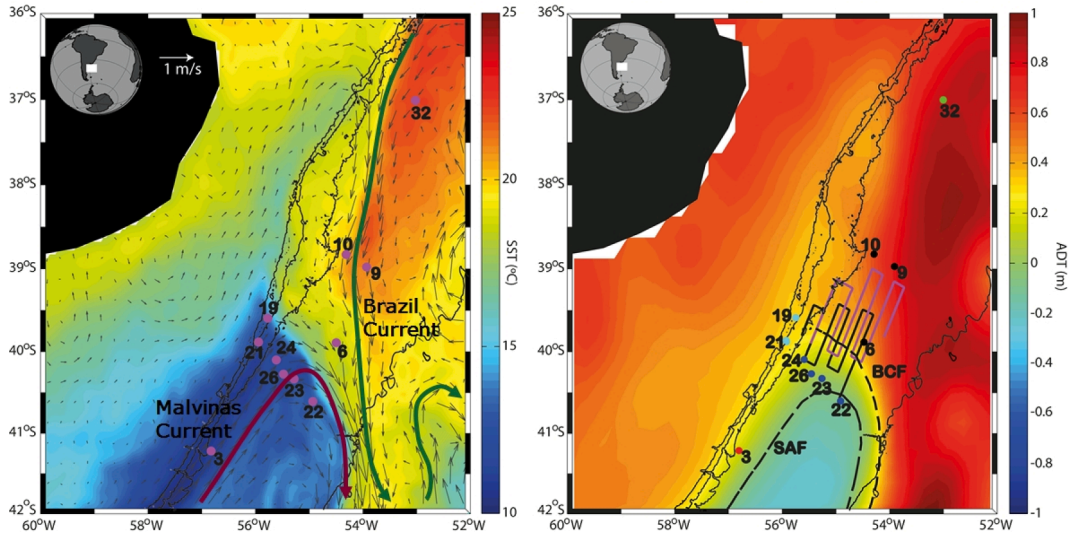

Fig. 1. Surface view of the BMC during the rETRO-BMC cruise, 8 to 28 April 2017. (a) Mean SST (coloured) and surface geostrophic velocities (grey vectors) as obtained from gridded altimetry, with the axes of the Brazil and Malvinas Currents sketched as solid purple and olive thick curves, respectively. The black lines correspond to the 200, 500, 1.000, and 5.000 m isobaths (GEBCO, 2008), and the microstructure stations are numbered. (b) Absolute dynamic topography (ADT) overlapping the isobaths with the Brazil Current Front (BCF) and Subantarctic Front (SAF) shown as dashed lines. The SeaSoar tracks during 17–18 April (black line) and during 19–21 April (magenta line) are shown. The stations are coloured according to locations: upstream the BC (32), north of the front (6, 9, 10), south of the front (22, 23, 24, 26), over the continental slope (19, 21) and along the MC (3). The SST is obtained from the global ocean Sea Surface Temperature and Sea Ice Analysis (OSTIA) and the ADT and surface geostrophic velocities come from the DUACS delayed-time altimeter gridded maps provided by the Copernicus Marine Environment monitoring service.

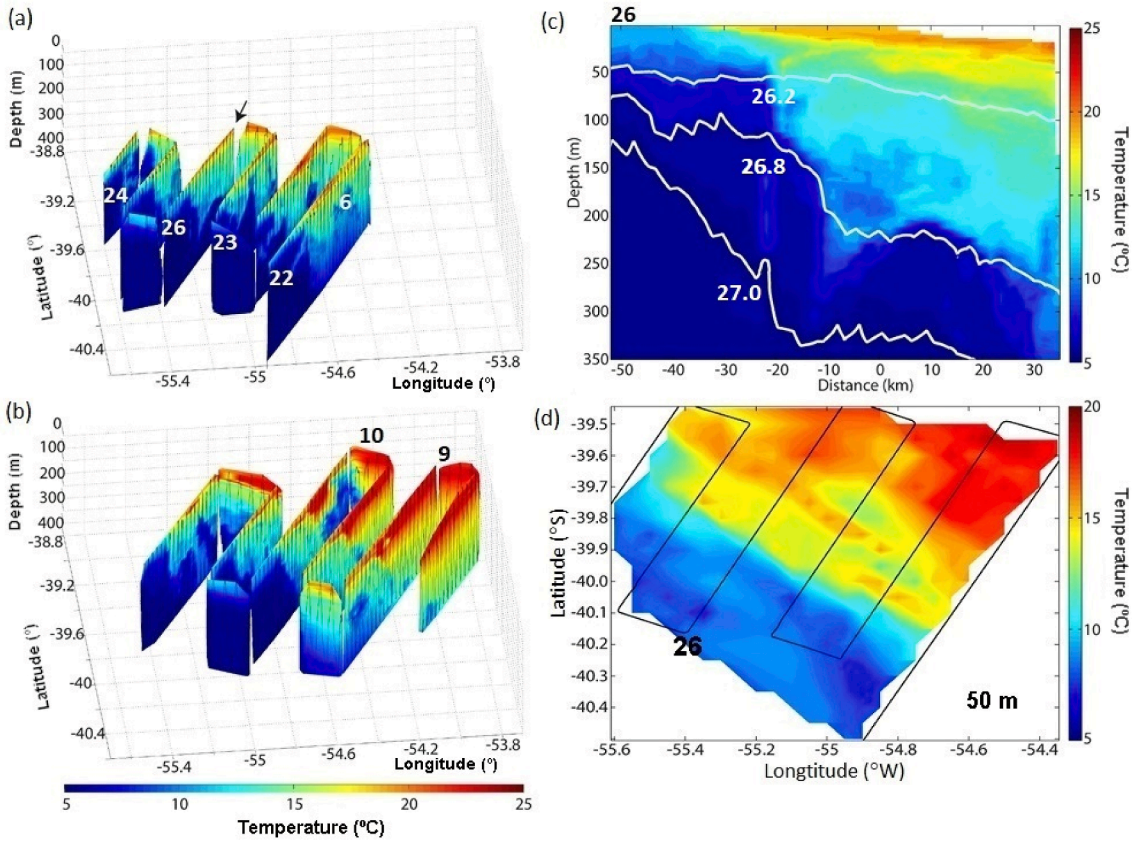

Fig. 2. (a and b) Three-dimensional temperature as viewed during the SeaSoar1 and SeaSoar2 transects (17–18 April and 19–21 April, respectively); SeaSoar1 went through or close to stations 22, 23, 24 and 26 about one day before microstructure measurements and through station 6 about four days after; SeaSoar 2 went close to stations 9 and 10 about five days after the microstructure measurements (adapted from Orúe-Echevarria et al., 2019a). (c) Vertical section of the temperature along the SeaSoar1 transect marked with an arrow in (a); the white lines represent selected potential density contours (26.2, 26.8 and 27.0 kg m^{-3}). (d) Horizontal section of temperature at 50 m as obtained during SeaSoar1.

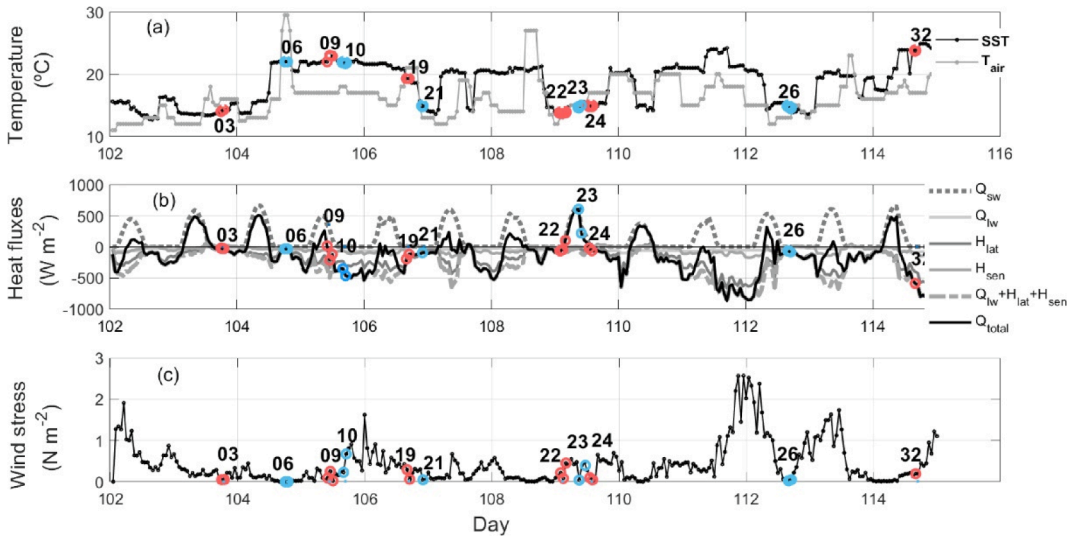

Fig. 3. Meteorological variables during the microstructure measurements, starting from day 102 (12 April 2017). The station numbers are indicated in black and correlatively highlighted with red and blue dots to distinguish the consecutive stations. (a) Air and surface sea water temperatures; (b) the components of total heat flux, Q_{total}: Q_{sw} incoming short wave radiation, Q_{lw}, long-wave radiation, H_{lat}, latent and H_{sen}, sensible heat fluxes and the sum $Q_{lw} + H_{lat} + H_{sen}$; (c) total sea surface wind stress.

Table 2
Ranges of the friction velocities and buoyancy fluxes during the time intervals when the microstructure casts were performed.

Station	u* (10^{-2} m s^{-1})	J_b (10^{-8} W kg^{-1})
03	[0.73, 1.05]	[-1.37, −1.90]
06	[0.13, 0.14]	[-1.77, −2.07]
09	[0.50, 1.58]	[-1.45, −14.4]
10	[1.51, 2.57]	[-20.1, −26.7]
19	[0.79, 1.71]	[-7.14, −12.02]
21	[0.71, 0.71]	[-5.35, −5.35]
22	[0.92, 2.11]	[-3.98, 4,63]
23	[0.65, 2.16]	[30.3, 30,4]
24	[0.70, 1.00]	[-1.16, −3.20]
26	[0.52, 0.72]	[-3.89, −4.95]
32	[1.39, 1.39]	[-34.1, −34.1]

continuous mode (every 6 s). Based on these data, the wind stress, the sensible and latent heat fluxes and the net long wave heat flux have been computed using the standard bulk formulas implemented on the sea-mat/air-sea toolbox for Matlab (https://github.com/sea-mat/air-sea). The short wave radiation into the sea was computed using the Zillman (1972) equation for radiation under cloudless skies, which considers the air vapour pressure (Lengfeld et al., 2010), corrected for the cloudiness according to the formula proposed by Payne (1972). In Fig. 3 the air and sea temperatures, the different components of the total heat flux and the wind stress are presented.

The front was repeatedly crossed during the cruise, moving from regions where the water temperature was up to about 5 °C higher than the air to others where this difference was considerably lower or even opposite (Fig. 3a). Most of the stations were sampled during the night and only stations 09 and 23 were sampled during the day. Station 22 was recorded at dawn and station 24 at dusk. Net heat flux was close to zero or slightly negative in almost all stations, except in stations 10 and 32 where negative fluxes were>300 W m^{-2} and in station 23 where the total flux was positive (Fig. 2b). The sea-surface wind stress was always<0.5 N m^{-2}, except in station 10 (Fig. 3c) where it was at the limit for working conditions and only one profile was recorded. Station 26 was sampled under calm conditions following strong winds.

The maximum and minimum values of the friction velocity u_* and the buoyancy flux J_B are calculated for the time periods of measurements (Table 2). The friction velocity is computed from the wind stress τ and the sea surface density ρ_0, according to $u_* = \sqrt{\tau/\rho_0}$. The buoyancy flux is computed from the net heat flux, Q_T as $J_b = \frac{g\alpha Q_T}{\rho C_p} + g\beta S(E-P)$, where $\rho$and S have been taken as the density and salinity at the sea surface, c_p is the specific heat for the seawater and α and β are the thermal expansion and saline contraction coefficients. E is the evaporation and P the precipitation. Precipitation was absent during measurements, and evaporation is calculated as $E = H_L/\rho L_v$ where L_v is the latent heat of vaporization for the seawater.

2.3. Hydrophysical measurements

The microstructure data were recorded with a falling profiler MSS-90 from Sea and Sun Technology (Prandke et al., 2000). It contains two small airfoil probes PNS6 with vertical resolution limited to 2 cm due to sensor geometry and one fast thermistor NTC with a sensitivity of 10^{-3} °C and response time of 7 ms. There are also standard pressure and precision conductivity-temperature (CT) sensors, which were calibrated before the campaign by the manufacturing company. The profiler was deployed on the windward side of the drifting ship, hence minimizing any turbulence associated with the vessel. The sampling rate of the profiler is 1000 Hz but CTD data were averaged every 10 points. The falling speed was around 0.7 m/s. Potential density is computed from pressure, conductivity and temperature using the UNESCO EOS 80 algorithm implemented in the CSIRO seawater toolbox (Morgan, 1994). Previously, a standard recursive filter (Lueck and Picklo, 1990) is applied to conductivity in order to avoid artificial spikes in the salinity which would contaminate the density profile. Sigma-theta is calculated as $\sigma = \rho - 1000\left[kgm^{-3}\right]$.

At each station, together with the microstructure casts, velocity data were also obtained with a RDI Workhorse Monitor lowered acoustic Doppler current profiler (LADCP) mounted on a rosette, consisting of a dual-head set-up used in synchronized mode, with a working frequency of 300 kHz and set to obtain velocities in 4-m bins. Data were processed with the Matlab LDEO IX toolbox (https://www.ldeo.columbia.edu/~ant/LADCP/) which uses CTD, vessel's navigation and bottom-tracking data. Simultaneously with LADCP measurements, conductivity-temperature-depth (CTD) data were obtained with a Sea-Bird Electronics multiparametric probe (SBE 911 +), which was accompanied by other sensors, such as dissolved oxygen. The probe sampled at a rate of 24 measures per second and was vertically averaged at 4 m to fit the

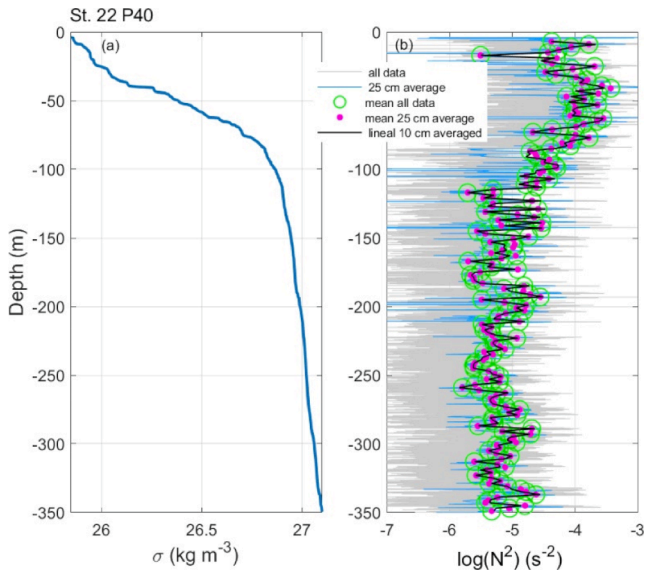

Fig. 4. Density and buoyancy frequency from microstructure data, as illustrated for cast P40 in station 22. (a) Sorted sigma profile. (b) Logarithm of the squared buoyancy frequency, log(N^2), as obtained through different methods: from the point to point gradient of the non-sorted density profile (grey line) or from the gradient of the density averaged every 25 cm (blue line) and afterward averaging the gradients over 2-m segments (green circles and magenta dots); or averaging the sorted density every 10 cm and calculating the density slope within segments of 2 m (black line).

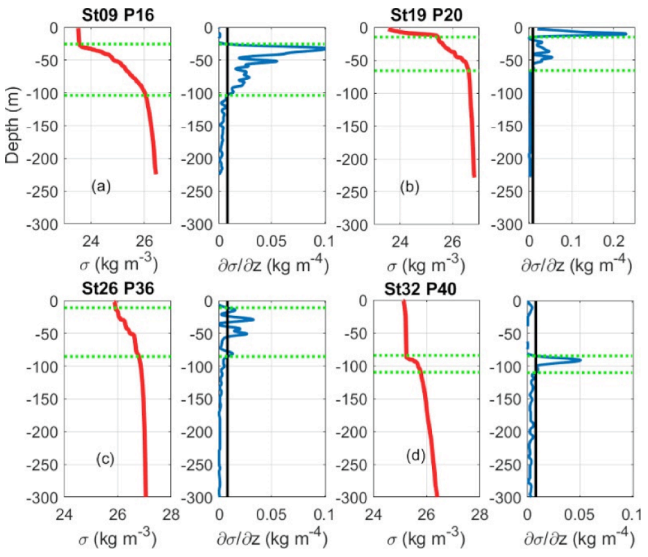

Fig. 5. Application of a density-gradient criterion to four casts (station and cast number as indicated), used to establish the upper and lower limits of the seasonal pycnocline. The sigma profile (red) and its vertical gradient after applying a low-pass filter with a cut-off of 1.5 m (blue) are presented; the vertical black line corresponds to the threshold value of 0.008 kg m^{-4} and the horizontal green lines set the limits of the seasonal pycnocline as determined by the method.

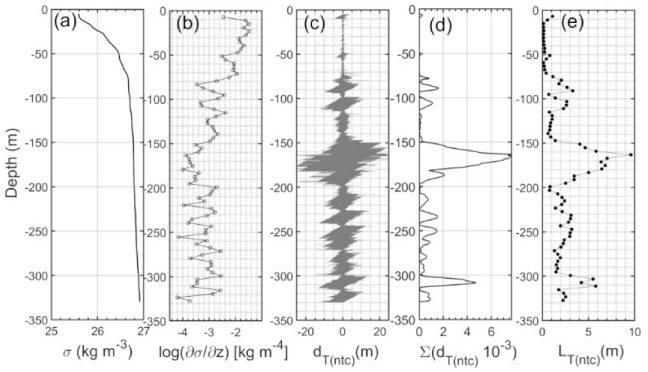

Fig. 6. Cast P25 recorded at station 21. Profiles of (a) potential sigma σ, (b) the logarithm of the sigma gradient,$log(\partial\sigma/\partial z)$, (c) the Thorpe displacements, $d_{T(ntc)}$, computed from the fast response temperature *NTC*, (d) the accumulated vertical addition of $d_{T(ntc)}$ and (e) the Thorpe scale, $L_{T(ntc)}$.

velocity intervals, using the Sea-Bird Electronics Data Processing software (https://www.seabird.com/software). In this article, the LADCP and CTD SBE data are only used for the computation of the Richardson number.

In the following, flow and turbulence variables used in the paper are described and the procedures followed to obtain them are presented in detail.

3. Methods

3.1. Brunt–Väisälä frequency

The stratification of the water column is characterized by the square of the buoyancy or Brunt–Väisälä frequency $N^2 = -\frac{g}{\rho_0}\frac{\partial\rho}{\partial z}$, where z is the vertical coordinate, g the gravity acceleration and ρ the potential density. Followings the standard method included in the seawater subroutines, N^2 has been calculated from the point to point density gradients as obtained from the microstructure data and then averaged within segments of several different thickness (0.5 m, 1 m, 2 m, 4 m and 5 m). These results are almost equal to values obtained either averaging the density data every 25 cm previous the gradient calculation or averaging the sorted density every 10 cm and calculating the density slope within each data segment (Fig. 4).

3.2. Limits of the seasonal pycnocline

The surface mixed layer and the underlying seasonal pycnocline are those portions of the water column that experience the direct influence of the atmosphere, usually expressed in terms of daily to seasonal variability. Below the seasonal pycnocline we find the permanent (or main) thermocline, which is the region indirectly affected by the atmosphere through either wind-induced downwelling-upwelling (subduction or obduction, respectively) or buoyancy-induced deep-winter convection (Sprintall and Cronin, 2011). In most ocean locations, such as the BMC, the thermocline coincides largely with the pycnocline; hence, hereafter we will refer indistinctly to thermocline or pycnocline.

We have determined the upper and lower depths of the seasonal pycnocline, which is the region that displays maximum vertical stratification, based on the gradient of the filtered sigma profiles. The sigma profile displays substantial variability, in some stations with step-like structures that can be>10 m (Fig. 5c). Hence, we have applied a low-pass filter of 1.5 m to the sorted sigma profile and have used a threshold value of 0.008 kg m^{-4} for the density-gradient profile. Examples of the results obtained for four profiles recorded at different representative stations are shown in Fig. 5. A single exception occurs in station 19 (Fig. 5b) where the first oscillation in the sigma gradient has not been considered when applying the threshold.

3.3. Thorpe scale

The vertical extension of the turbulent overturns is characterized by the Thorpe scale, L_T, defined as the root mean squared of the Thorpe displacements, d_T. The Thorpe displacements are calculated as the distance that each water parcel has to move vertically, up or down, in order

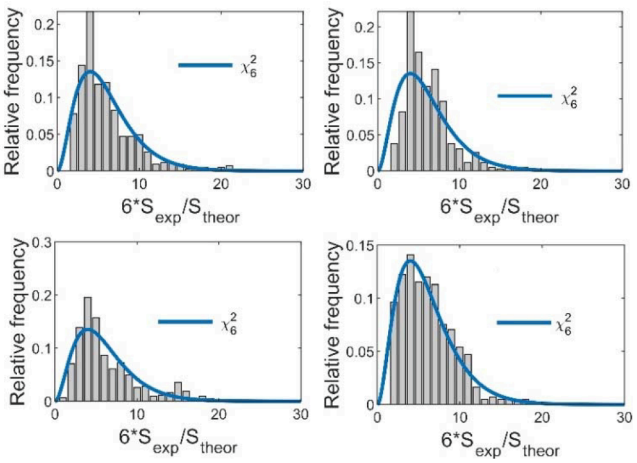

Fig. 7. Histogram of the ratio of the spectra computed from the recorded small-scale shear data (S_{exp}) with the Panchev-Kesich model (S_{theor}) and the theoretical χ^2_6 pdf (blue line) for 4 aleatory segments of 30 m length.

to obtain a density profile which increases monotonically with depth, assumed to be the initial stable profile over which turbulence develops (Thorpe, 1977). The density resolution that comes from CT precision sensors does not allow obtaining the Thorpe scale for relative low stratification. However, in some locations the mean temperature profile changes also monotonically in depth so the Thorpe displacements can also be obtained reordering the temperature profile. For this purpose, the fast response temperature profile, *NTC*, which has a resolution ten times higher than the precision temperature, is used. In this study, only at stations 19 and 21 there were no intrusions observed and the temperature profiles decrease monotonously with depth, and so the Thorpe scale can be computed.

An example of Thorpe scale calculation is presented in Fig. 6. Fig. 6a and 6b show the vertical distribution of potential density and potential density gradient, respectively. In Fig. 6c, the largest values of $d_{T(ntc)}$ are about $\pm$ 20 m and are observed between 150 and 200 m depth, coinciding with a weakly stratified portion of the water column (Fig. 6b). In Fig. 6d, the accumulated addition of $d_{T(ntc)}$ is presented. Based on this addition, the individual turbulent overturns can be identified because when the turbulent patches are independent from each other the accumulated addition goes to zero (Mater et al., 2015). Note the correspondence between the values of the cumulative addition and the patch structure of the displacements (Fig. 6c,d). Patch distribution is an important variable typically associated with significant local fluxes (Planella Morato et al., 2011; Cui et al., 2018).

Based on the Thorpe scale, the available potential energy (APE) of the turbulent instabilities in the density profile can be estimated as $N^2L_T^2$. Because the decaying time of the instability can be considered $\tau\ N/8$ (Smyth and Moum, 2000), the rate of APE to turbulent kinetic energy (TKE) transformation is expected to be $\sim .N^3L_T^2/8$

3.4. Dissipation rate of the turbulent kinetic energy

The amount of TKE per unit mass that is dissipated by the viscous stresses per unit time, ε, is obtained by comparing the small-scale shear spectrum with the one-dimensional (1D) theoretical Panchev-Kesich model (Gregg et al., 1996). We obtain the best fits by adapting the maximum likelihood spectral method proposed by Ruddick et al. (2000) to the Panchev-Kesich spectra (Roget et al., 2006, 2007). In this case, the TKE dissipation rate, ε, is the only fitting parameter.

Following Ruddick et al. (2000), we assume that the statistical variability of the fit follows a chi-squared distribution with d degrees of freedom, χ^2_d, which can be tested by comparing the ratio of the experimental spectra and the Panchev-Kesich theoretical spectra with the theoretical probability distribution. The variability of the fit agrees well with a chi-squared distribution with 6 degrees of freedom (Fig. 7). Therefore, we use the χ^2_6 probability distribution to obtain the likelihood function, which has a single maximum.

To quantify the goodness of this fit, we used the median absolute deviation (MAD) of the ratio between the experimental and theoretical spectra within the data domain. Ruddick et al. (2000) proposed a threshold equal to 2 $(2/d)^{1/2}$, where d are the degrees of freedom of the chi-squared distribution which follow the statistical variability of the data (d = 6 in our case). For a more precise fit we reduced the threshold

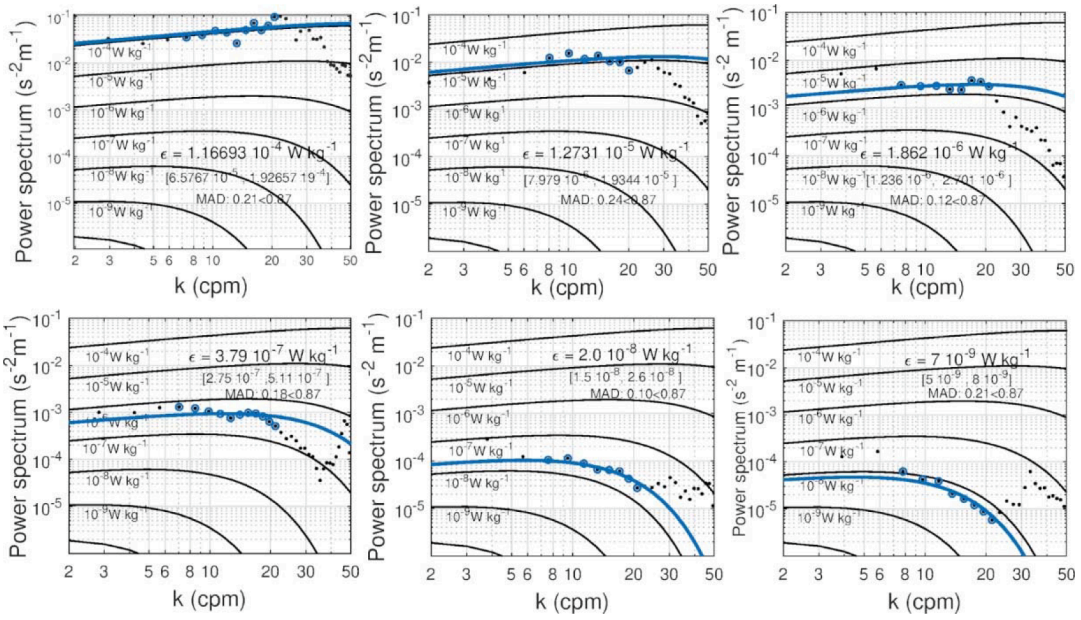

Fig. 8. Examples of the dissipation rates using the maximum likelihood spectral method to fit the Panchev-Kesich model (black curves). The best fits are shown in blue and the corresponding dissipating rates, the 95 % confidence limits and MAD are indicated; the data points used to fit the model are shown in blue. The examples correspond to 2-m segments centred at (top panels) 13 m in station 19 (*P*21), 64 m in station 32 (*P*31), 177 m in station 22 (P20), and (bottom panels) 205 m in station 26 (P35), 215 m in station 23 (*P*31) and 122 m in station 21 (P26).

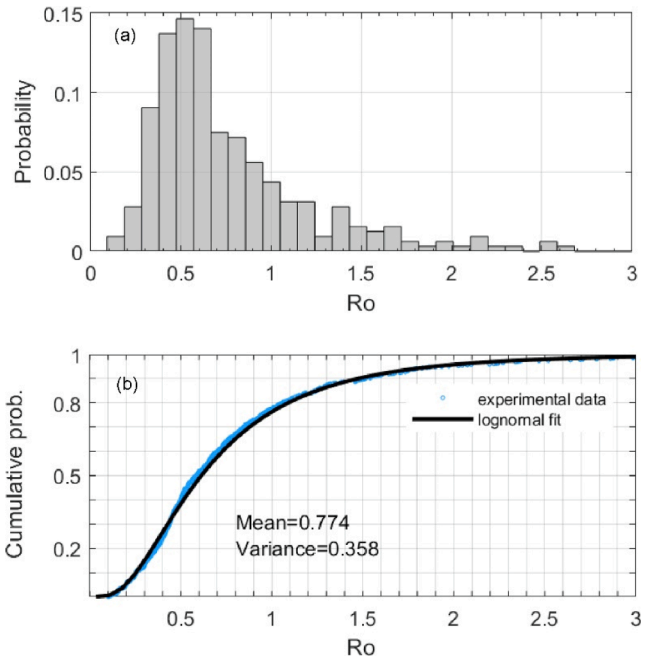

Fig. 9. Statistical representation of $R_O = L_o/L_T$ computed every-two metres for all casts at stations 19 and 21. (a) Histogram and (b) cumulative distribution of both the measured Ro and the data fit to the lognormal distribution.

to 1.5 $(2/d)^{1/2}$, which in our case is 0.87.

The theoretical Panchev-Kesich spectra for different dissipation rates, ranging from 10^{-9} to 10^{-4} W kg^{-1}, are represented in Fig. 8. Furthermore, the experimental shear spectra for 2-m segments are also represented. The profiler generates eddies of approximately its own length but only those of half its length can be resolved (Nyquest frequency). Accordingly, for the spectral analysis a window of 512 points has been used which considering a falling speed of 0.7 m s^{-1} correspond to a length of about 0.35 m. The transformation from frequencies to wavenumbers has been done considering the mean falling velocity of the probe at each segment so the wavenumber data points are not exactly the same in all plots.

As observed from the different panels in Fig. 8, in some segments the power of the spectra is higher than the theoretical spectra at scales>20 cm, indicating some contamination; further the statistical significance of the smallest wave numbers is low. On the other side of the spectra, at scales below 4.5 cm, for high dissipation rates the response of the sensor decreases and the noise dominates at low dissipation rates. Accordingly, to standardize our analysis we restricted the fitting range from 6 cpm to 22 cpm.

In this study, the dissipation rates below 5 m depth have been computed for all profiles fitting the shear spectra for segments of either 1 or 2 m, showing consistent results. In particular, between 5 and 11 m there are 27 spectra fits (out from 5587) giving ε 10^{-3} –10^{-2} W kg^{-1}, which fulfil the MAD threshold criteria and satisfy visual inspection, so there is no objective criteria to reject them although some contamination can't be completely disregarded. In the following section, the values of ε obtained by fitting the small-scale shear spectrum are compared to indirect estimates.

3.5. Ozmidov scale and indirect estimations of ε

The Ozmidov or buoyancy scale, defined as $L_O = \varepsilon^{1/2}N^{-3/2}$, is a theoretical estimation of the length scale where buoyancy and inertial forces balance. This scale represents the maximum vertical extension where turbulence is not influenced by the background stratification. In this study L_O has been computed using N^2 obtained from the micro-

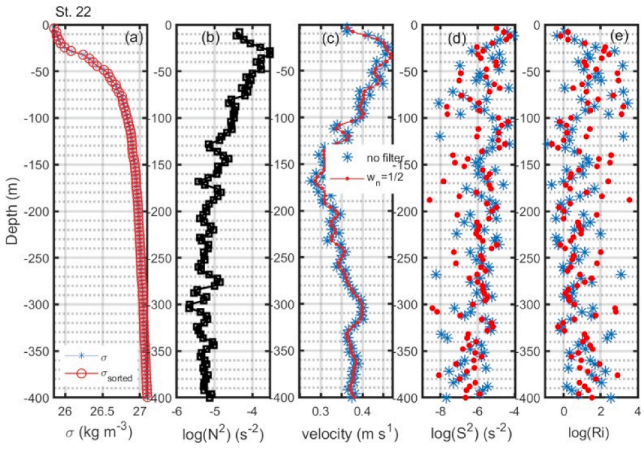

Fig. 10. Example of calculation of the Richardson number from the SBE-CTD and LADCP data with a vertical resolution of 4 m. (a) Measured sigma and sorted sigma profiles. (b) N^2 computed directly from the gradient of density between consecutive data points. (c) Original velocity dada measured every 4 m (blue stars) and after being filtered with a cut-off of 8 m (2 points) (red dots). (d) Shear squared as computed from the two velocity data presented in previous panel. (e) Corresponding Richardson numbers. Colours are coherent with previous panels: blue, no filter; red, 2 points filter.

structure profiler data (section 3.1).

In active shear driven turbulence, including Kelvin-Helmholtz instabilities with relatively small overturns, it is well accepted that L_O aL_T (Mater et al., 2015) where a = 0.8 (Dillon, 1982) is usually taken, although other authors have found values ranging between 0.35 and 1.55 (Crawford, 1986; Wesson and Gregg, 1994; Ferron et al., 1998). In general, bulk averages agree with L_T L_O and, accordingly, the dissipation rate can be estimated from the Thorpe scale following $\varepsilon \cong \varepsilon_T = 0.64L_T^2N^3$.

For all the casts recorded at stations 19 and 21 (where the Thorpe scale can be computed, recall section 3.3), the ratio of the Ozmidov and Thorpe scales, $R_0 = L_O/L_T$, has been obtained for 2-m segments. With the aim to indirectly test the values of the low dissipation rates computed from the small scale shear, the statistics of $R_O$for those segments where $\varepsilon < 10^{-6.5}$W kg^{-1} is presented in Fig. 9. The cumulative probability fits a lognormal distribution with a mean value of 0.77, close to the canonical value of 0.8 (Fig. 9b). These results support the values of the dissipation rates computed from the small-scale shear signal (Section 3.4).

3.6. Corrsin scale and gradient Richardson number

The Corrsin or shear scale is defined as $L_C = \varepsilon^{1/2}S^{3/2}$ where $S = \partial U/\partial z$ is the mean flow shear. L_C is approximately the minimum length where the background shear starts feeding the turbulence field. As already commented, for stratified shear flows, buoyancy starts suppressing the turbulence at a vertical scale of about L_O, so sheared turbulence is expected to be generated from the mean flow on the scales ranging approximately between L_C and L_O.

In stratified sheared flows, the gradient Richardson number, defined as $Ri = N^2/S^2$, compares the suppression of turbulence by vertical stratification to shear production by the mean flow. A critical value, Ri_{cr}, is usually considered to determine the conditions where background stratification does not prevent shear instabilities from developing.Ri_{cr} is usually considered equal to 1/4 (linear stability, Miles, 1961). Thorpe and Liu (2009) suggested that real flows can be in a marginal stability state where, recursively, external forcing tend to strength the shear until it becomes instable but turbulence deaccelerates the shear making the flow stable. Practically, Ri values depend on how the gradients are calculated. Based on laboratory experiments, Smyth and Moum (2000)

proposed critical numbers between 0.32 and 0.45. Note that $Ri = N^2/S^2 = (L_C/L_O)^{4/3}$ so $Ri_{cr} < 1$ also indicates that, in stratified shear flows, turbulence is produced in the scales larger than L_C and smaller than L_O. However, for Kelvin-Helmholtz (KH) instabilities $Ri_c \cong 1$ and for Hölmböe instabilities $Ri_c \cong 3$ (Strang and Fernando, 2001).

The values of N^2used in the Ri computation are obtained based on the point to point density gradient as obtained from the SBE-CTD measurements with the same resolution as the LADCP. Although the LADCP velocity data are averaged every 4 m and data quality is good, there are some profiles where the velocity values show intermittent high oscillations. In a first analysis, previous to the computation of the Richardson number, we used a Butterworth filter with a cut-off $w_n = 1/2$ (2 points; 8 m). However, as expected, even a very slight filtered velocity modifies the sharp velocity interfaces and the corresponding shear, modifying the local Richardson numbers by more than one order of magnitude (Fig. 10).

The depth intervals with high velocity fluctuations often coincide with regions of high turbulence. Accordingly, we decided to recalculate the shear without filtering the velocity profiler. Although there are local differences when computing Ri from original or filtered velocity data (Fig. 10e), the general statistics are very similar.

3.7. Kolmogorov scale and buoyancy Reynolds numbers

The Kolmogorov scale $L_K = \left(\nu^3/\varepsilon\right)^{1/4}$ is the approximately scale where turbulence starts to be affected by viscous dissipation produced by the small-scale stresses. The Buoyancy Reynolds number is defined as $Re_b = \varepsilon/(\nu N^2)$ and compares the destabilising effect of the turbulence to the stabilising effect of stratification and viscosity. Note that $Re_b = (L_O/L_K)^{4/3}$ so that only when $Re_b > Re_{bcr}$ the turbulence is considered active; Re_{bcr} has been established to be between 15 and 30 (Rohr et al., 1984; Gibson, 1991). We calculate Re_b within segments of 2 m from the corresponding values of ε and N^2 and considering the dependence of the viscosity on the temperature and salinity.

3.8. Overturn (or turbulent) Froude and Reynolds numbers

Considering that turbulent scales are computed from microstructure profile measurements recorded at some random stage of the measured turbulent overturn, the state of the turbulence can be analysed based on the overturn Froude number $Fr_T = \left(\varepsilon/\left(N^3 L_T^2\right)\right)^{1/3} = (L_O/L_T)^{2/3}$ and the overturn Reynolds number $Re_T = \left(\varepsilon^{1/3} L_T^{4/3}/\nu\right) = (L_T/L_k)^{4/3}$ which compare the Thorpe scale with the Ozmidov and Kolmogorov scales, respectively. Note that $Fr_T = (Re_b/Re_T)^{1/2}$. Maffioli et al. (2016) argued that for sufficiently high $Re_b$the most appropriate measure to generically parametrize mixing is Fr_T.

Ivey and Nokes (1989) showed that viscosity suppresses the turbulence when $Re_T \leq 15$. In general, for $Re_T > 15$ when $Fr_T < \left(\frac{Re_{bcr}}{Re_T}\right)^{1/2}$ the viscosity also supresses turbulence (here Re_{bcr} is the critical Reynolds number). It is commonly accepted that shear instabilities retain $Fr_T \cong 1$ at the time of maximum turbulent intensity (Peters et al. 1995; Kantha and Clayson, 2000). A scattering of the observations around $Fr_T \cong 1$is expected considering that there may be other sources of turbulence besides small scale shear instabilities (Imberger and Ivey, 1991).

For the stations on the continental slope, $Fr_T$and Re_T have been computed from ε, N^2 and L_T calculted within segments of 2 m, and considering the dependence of ν on temperature and salinity. The representation of Fr_T as a function of Re_Thas been named a hydrodynamic diagram (Ivey and Imberger, 1991) or regime diagram (Portwood et al., 2016).

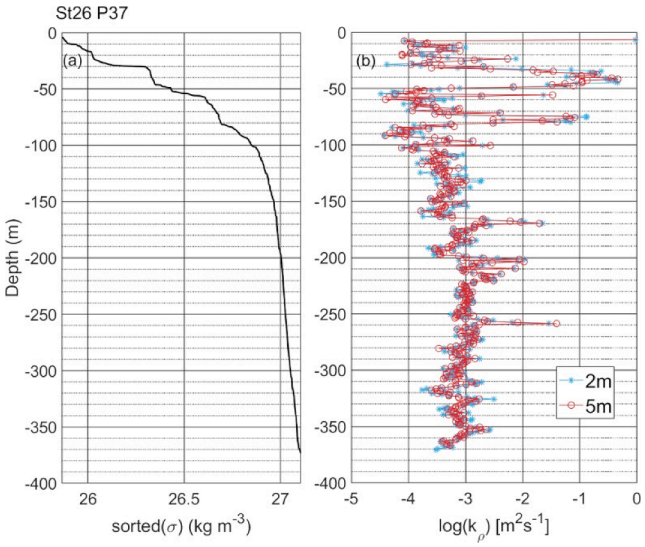

Fig. 11. (a) Sorted sigma for the cast P37 and (b) the corresponding diffusivities calculated every 2 m considering the 2-m segmentation for the computation of N^2 (blue), and considering a 5-m segmentation for the computation of N^2 (red).

3.9. Diapycnal eddy diffusivities

Following Osborn (1980), the diapycnal eddy diffusivities are calculated every 2 m as $K_\rho = 0.2\varepsilon/N^2$, with the buoyancy frequency characterizing the environment stratification calculated both over 2-m and 5-m segments (Fig. 11). In our data, computing N^2 in 5-m segments instead of 2-m segments decreases the mean diffusivities by a factor of 0.89 over the entire water column and by a factor of 0.88 in the seasonal pycnocline. The results presented in this paper correspond to this enlarged segmentation of N^2.

3.10. Turner angle

The Turner angle (Turner, 1973; Ruddick, 1983) is an indicator of the stability of the water column to double diffusion. It is defined as $Tu = \tan^{-1}[(\alpha\overline{T}_z + \beta\overline{S}_z)/(\alpha\overline{T}_z - \beta\overline{S}_z)]$, where α is the thermal expansion coefficient, β is the saline contraction coefficient, and $\overline{T}_z$ and $\overline{S}_z$ are respectively the background temperature and salinity gradients.

When$Tu = 0°$, $\overline{S}_z > 0$ and $\overline{T}_z < 0$ so, the temperature and salinity gradients have both a stabilizing effect on the water column and contribute equally to the density gradient. From this point if either the absolute value of $\overline{S}_z$ or $\overline{T}_z$ decreases, $|Tu|$increases until $Tu = \pm 45°$, when the decreasing gradient vanish. If $\overline{S}_z < 0$ and $\overline{T}_z < 0$ – warm and salty water overlies cold and fresh water – then $45° < Tu < 90°$ and salt-fingering (SF) instabilities are favoured. On the other hand, if $\overline{T}_z > 0$ and$\overline{S}_z > 0$ – cold and fresh water overlies warm and salty water – then $-90° < Tu < -45°$ and the water column is susceptible to double-diffusive convection (DDC). The highest probability of SF or DDC occurs for Tu close to 90° or −90°, respectively. Finally, if $Tu > 90°$ or $Tu < -90°$, $\overline{S}_z < 0$ and $\overline{T}_z > 0$ – warm and fresh water overlies cold and salty water – the profile is gravitationally unstable.

Computation of the background gradients of T and $S$to obtain the Tu angle has been done from data obtained with the microstructure profiler after being interpolated every cm and passing a moving average low-pass filter with a 4-m window. Finally, the T and S vertical profiles were interpolated every 0.5 m.

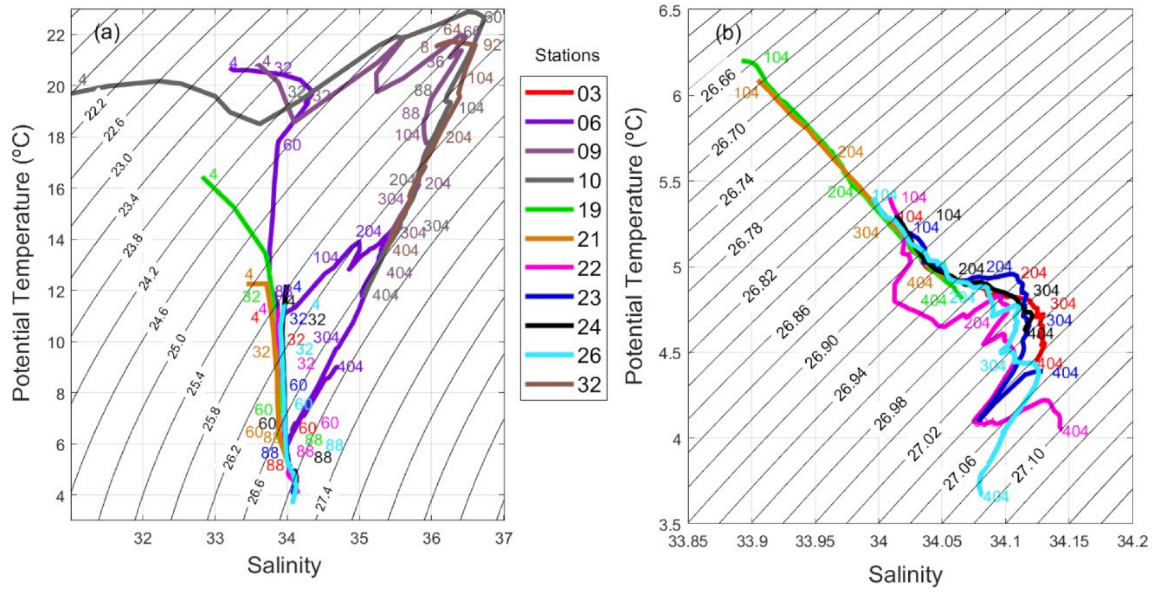

Fig. 12. (a) *T*-S diagram for the water masses at the different stations, identified by colour; depth values are also coloured by station (32, 60, 88, 104, 204, 304 and 404 m). (b) Detail of the *T*-S diagram for waters below 100 m. In both panels, the black thin lines correspond to the isopycnals.

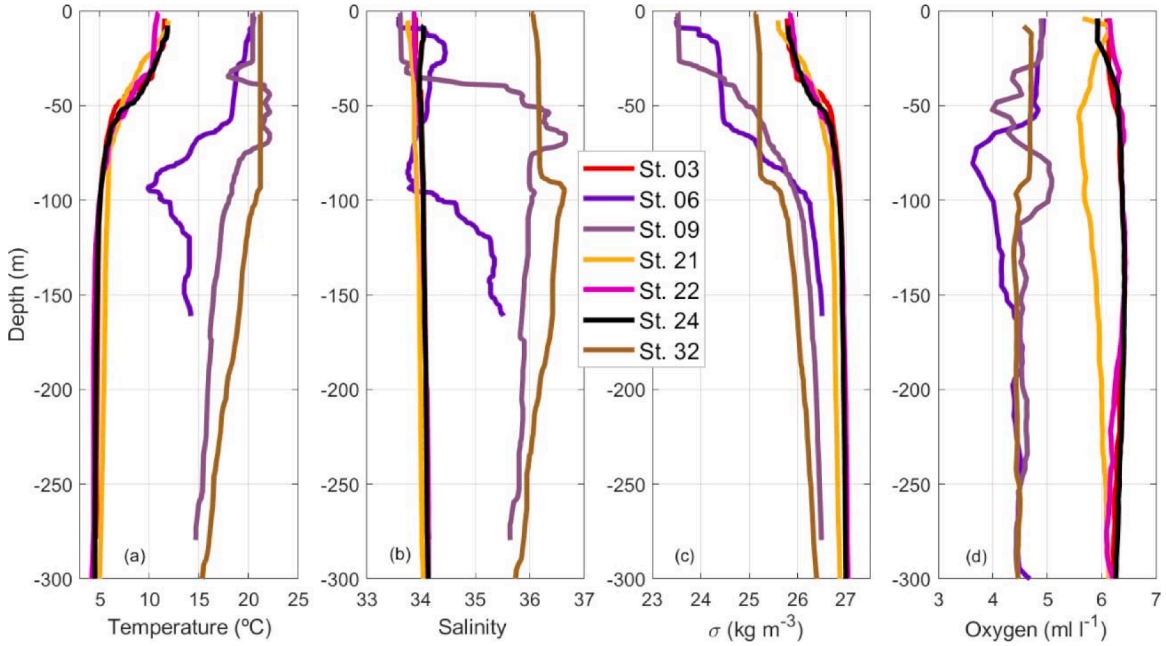

Fig. 13. Temperature, salinity, density and dissolved oxygen profiles in stations 03, 06, 09, 21, 22, 24 and 32. All profiles correspond to selected casts of the microstructure probe, except for the dissolved oxygen that comes from the SBE cast.

4. Observation site at the time of measurements

4.1. Water masses

The temperature-salinity diagrams (Fig. 12) clearly illustrate that the BMC region represents a crossroads between waters of subtropical, subantarctic and shelf origin. In station 32 upstream the BC, and in stations 9 and 10 located north of the front, the upper part of the water column is occupied by Subtropical Shelf Waters ($T > 18.5$, $S < 36.0$; Piola et al., 2000; Möller et al., 2008), which are shelf waters formed by the dilution of BC waters with coastal origin waters, and with the contribution of river water from Rio de la Plata ($S < 33.6$; Berden et al., 2020). In the 50 to 100 m depths, we find the warmest and saltiest ($T > 19$ °C, $S > 36.38$) Tropical Water (TW), formed at tropical latitudes and advected within the BC. Below and down to 400 m, we find South Atlantic Central Water (SACW), characterized by a straight line in the *T*-S diagram between (12.0 °C, 35.4) and (18 °C, 36.2) (Valla et al., 2018; Orúe-Echevarría et al., 2021).

Stations 19 and 21, located over the continental slope, display the same vertical arrangement of water masses as those stations located south of the front (22, 23, 24, 26) and along the BC (03), but with the influence of the summer shelf Patagonian waters (slightly warmer, T > 4.8 °C, and fresher, S < 34.05, conditions down to 400 m); in stations 19 and 21 no intrusions are observed (Fig. 12b). Waters at stations 19, 21, 22, 23, 24 and 26 are of subantarctic origin, substantially fresher and colder than in those stations over the BC. The first 100 m of the

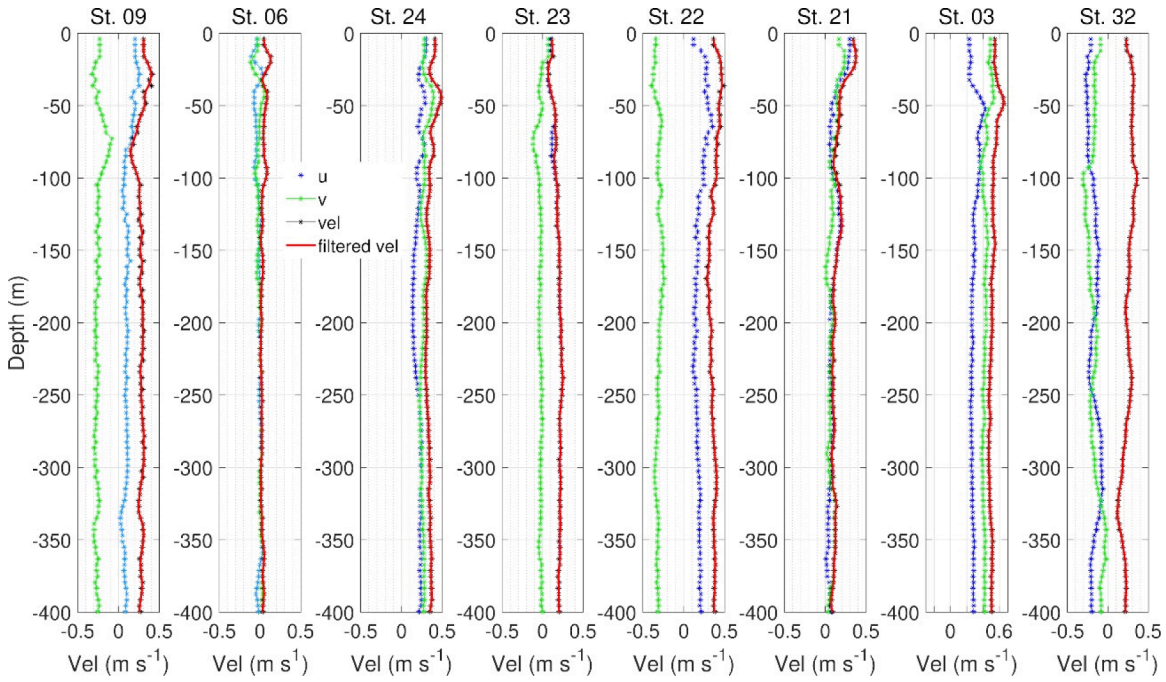

Fig. 14. Latitudinal (green) and zonal (blue) components of the velocity. The positive meridional and zonal velocities are northward and eastward, respectively. The absolute speed (modulus of the velocity vector) is also shown (red line).

water column are occupied by Subantarctic Shelf Water (SASW, $S \cong 33.8$) which flows along the Patagonian shelf from 55°S and is partly exported offshore close to the BMC (Franco et al., 2018, Berden et al., 2020). Immediately below, we find Subantarctic Mode Water ($T \cong 5.1$ °C, $S \cong 34.1$; Piola and Gordon, 1989) formed in deep winter convection along the Sub-Antarctic Zone of the northern Drake Passage (Paniagua, et al., 2018). The eastern stations, located over the retroflection of the MC (22, 23, 26), at depths below 100 m display high variability. This corresponds to the presence of intrusions as thick as 50 m during the cruise (Orúe-Echevarría et al., 2019). At station 06, an intense interleaving structure, formed by the two different types of water masses, can be identified.

In Fig. 13, several representative profiles of temperature, salinity and sigma, as obtained with the microstructure profiler, are presented. The oxygen vertical structure, as sampled with the SBE probe, is also presented, as it can be used as a tracer for these water masses. The warmer, saltier and lighter northern stations (06, 09 and 32) are also less oxygenated (<6 ml l^{-1}). The presence of continental water causes that these northern stations present substantial variability in the shallow (<100 m) layers.

4.2. Mean flow

During the campaign, the flow field displayed substantial spatial variability, with the maximum speed along the continental slope and the frontal system, and lower values on the northern side of the BMC (Fig. 14). A comparison with density profiles (Fig. 13) shows some clear associations in the more stratified stations. In station 9, located north of the BMC (Fig. 1), the speed is maximum and directed offshore in the surface layer (0.4 m s^{-1} at 28 m), decreases in the seasonal thermocline (0.15 m s^{-1} at 80 m) and increases again in the permanent thermocline but flowing along-slope to the southwest (mean speed about 0.3 m s^{-1}). In contrast, in station 6 there is an interleaving vertical structure composed by water masses of northern and southern origin, with fairly low speeds.

In those stations located south of the BMC, the flow velocity at each station was fairly constant in depth, with velocities up to about 0.5 m s^{-1}. This can be observed in stations 24, 23 and 22, which are located along a section normal to coast, with stations 24 and 22 closest and farthest offshore, respectively. Station 21, which is located over the continental slope, displays a maximum speed near the sea surface (0.37 m s^{-1} at 16 m) and a subsurface secondary maximum (0.2 m s^{-1} at 134 m). Finally, stations 03 and 32, located along the MC and upstream the BC, display fairly large and vertically-homogeneous speeds (0.5 m s^{-1} and 0.25 m s^{-1}, respectively).

4.3. Vertical stratification and shear

Our study covers the upper portion of the water column: the surface mixed layer, the seasonal pycnocline, where stratification reaches maximum values, and the upper part of the permanent pycnocline. The upper and lower limits of the seasonal pycnocline are determined for each cast based on the gradient of the filtered sigma profiles (section 3.2) and the mean values at each station are presented in Table 3.

A joint view of mean values of the stratification, absolute velocity, velocity shear and Richardson numbers for both the seasonal and permanent pycnoclines (down to 400 m) is presented in Fig. 15. All values are based on data recorded with the LADCP and SBE with a vertical resolution of 4 m, so statistics are computed for 10–20 data points in the seasonal pycnocline and from about 80 points in the permanent pycnocline (Table 3).

In the seasonal pycnocline N^2 $10^{-4}s^{-2}$, one order of magnitude

Table 3
Upper and lower limits of the seasonal pycnocline.

Stations	03	06	09	10	19	21	22	23	24	26	32
$H_{upp}(m)$	20	<6	23	10	17	11	24	12	12	<6	83
$H_{low}(m)$	62	99	103	93	65	69	78	78	78	88	109

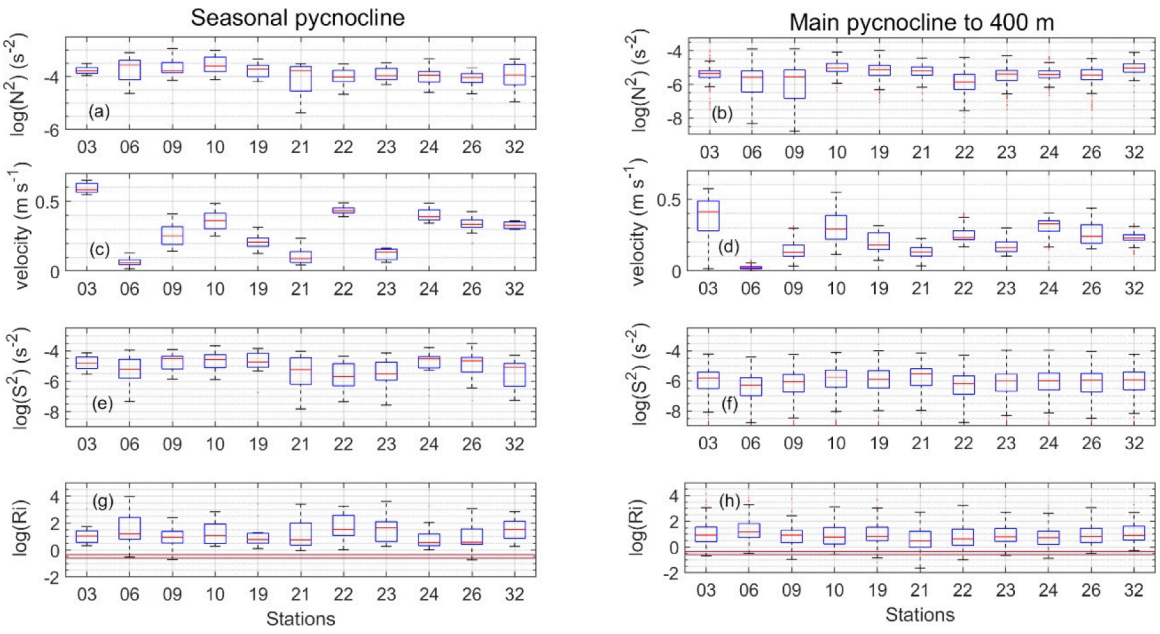

Fig. 15. Box plots of the squared buoyancy frequency, the speed, the squared velocity shear and the Richardson number within the seasonal pycnocline and in the permanent pycnocline down to 400 m, based on LADCP and SBE data. The edges of each box are the 25th and 75th percentiles, the whiskers extend to the most extreme data not considered outliers; outliers are shown with red dots. In the Richardson number panels the red horizontal lines stands for Ri_{cr} = 0.25and 0.45.

higher than in the permanent pycnocline, where N^2 $10^{-5}s^{-2}$ (Fig. 15a, b). For each station, the velocities at the seasonal and permanent pycnoclines are fairly similar (Fig. 15c, d), ranging from about 0.5 m s^{-1} at station 03 in the MC to<0.1 m s^{-1} at station 06, north of the front. The corresponding shear in the permanent pycnocline (Fig. 15e), S^2 $10^{-5}s^{-2}$, is larger than in the permanent pycnocline, where S^2 $10^{-6}s^{-2}$ (Fig. 15f).

In Fig. 15g, h the statistics of the Richardson numbers are compared with the 0.25 and 0.45 values, which are considered as critical for shear instability (section 3.6). In the permanent pycnocline, most stations show segments with Richardson numbers lower than the critical values (Fig. 15h), so we can conclude that there are favourable conditions for shear-induced turbulence. In the highly stratified seasonal thermocline, in contrast, there are few segments where $Ri < Ri_c$(Fig. 15g). Note that the Richardson numbers have been computed over a vertical scale of 4 m simply because velocity data at smaller scales are not available.

5. Energy dissipation

5.1. Dissipation rates of turbulent kinetic energy

Considering that only irreversible processes contribute to effective turbulent diapycnal diffusivities (Ma and Peltier, 2021), the intensity of mixing in each station can be assessed through the TKE dissipation rates as estimated for each individual cast. Fig. 16 illustrates the time evolution of these dissipation rates as inferred from the different microstructure casts done in four representative stations. The Richardson number, *Ri*, is computed from the density obtained from CTD sensors and the velocity recorded simultaneously from the LADCP (section 3.6) and also from N^2obtained with the microstructure profiler (section 3.1). The most relevant features in the contour plots are the high rates of dissipation within the upper ocean but away from the sea surface, and the existence of high-dissipation patches in the permanent pycnocline, with vertical extension ranging from several metres to a few tens of metres. Note that large thermohaline intrusions below 100 m show up in the *T*-*S* diagram (Fig. 12b), particularly in the stations 22, 23 and 26. Notice also that stations located on the continental slope are shallow (541 m in station 21) so that near-bottom mixing resulting from the breaking of internal waves can be expected.

The prevalence of relatively low *Ri* values points at an environment favourable to shear instability, although without clear correspondence between high dissipations rates and low *Ri* numbers. This may be due to the fact, already commented, that the vertical resolution of the velocity data used to compute *Ri* is low and that the microstructure measurements were done from a non-anchored ship between 1 and 4 h of difference with the velocity measurements, in a region where there is a high spatial and temporal variability of the flow. Turbulent events are expected to decay in times of the order of $\tau = 8N^{-1}$ so, for example, if $N^2 = 10^{-5}$ s^{-2} then $\tau = 0.7$ h, and the horizontal scales can be expected to be about 10 times larger than the vertical scales (Smyth and Moum, 2012). Non local balance between production and dissipation of TKE cannot be disregarded either (Nash et al., 2012; Lozovatsky et al., 2012).

5.2. Dissipation near the sea surface

The dissipation rates down to 120 m, obtained from all the cast at nine representative stations are shown in Fig. 17. The sigma profiles differ markedly between stations, often presenting layers typically several meters thick. In all stations, the velocity changes rapidly with depth throughout the seasonal pycnocline.

The dissipation rates peak near the sea surface and decrease rapidly with depth, probably reflecting the influence of the surface waves (Annis and Moum, 1995). Lozovatsky et al. (2005), based on data in the North Atlantic, proposed the curve $\varepsilon(z) = 0.184e^{-0.85z}$ to simulate the effect of surface waves in the near-surface turbulence, which shows good agreement with the data (Fig. 17).

For all stations, the wall law $\varepsilon(z) = 1.5u_*^2/(kz)$, where u_* is the friction velocity (Table 2) and $k = 0.4$ the von Karman constant, is also represented for every hour during measurements. Furthermore, in order to include the convective effect of the buoyancy flux J_B (Table 2), the curves $\varepsilon(z) = 1.5\frac{u_*^2}{kz} + 0.8J_B$ (Lozovatsky et al., 2005) are also plotted. These theoretical profiles seem to set the lower limit of the mean dissipation rates within the seasonal pycnocline, although dissipation rates as much as two orders of magnitude larger are observed.

The velocity profiles in Fig. 17 show the presence of high vertical shear, which may be the result of flow convergence at the frontal region (Fig. 2) and can lead to shear-driven mixing. Near the continental shelf

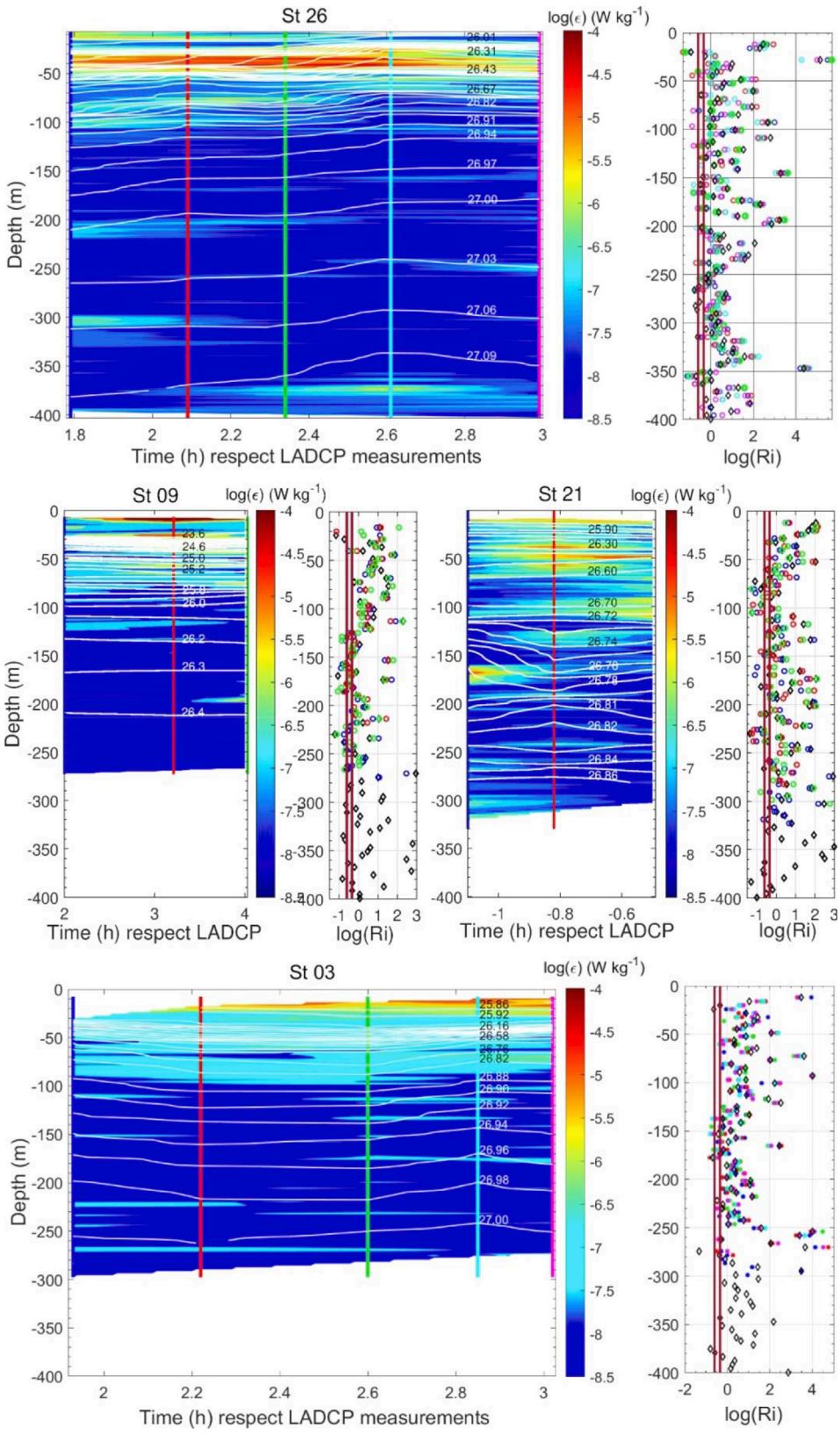

Fig. 16. Contour plots of the dissipation rates at stations 26, 09, 21 and 03. The time of measurements is indicated with vertical lines of different colours, referred to the time when LADCP measurements were performed; accordingly, negative times in station 21 indicate that the microstructure measurements were performed before the deployment of the LADCP. Isopycnals are plotted superimposed in grey colour. The black diamonds on the right panels stand for the Richardson numbers as computed with the velocity and density recorded simultaneously from the standard CTD and the LADC at t = 0. The coloured Richardson numbers dots stay for *Ri* computed using N^2 calculated from the microstructure casts (using the same colours as in the left panels); the vertical lines in the Richardson plots correspond to the values of 0.25 and 0.45.

break in the East China Sea, Matsuno et al. (2005) found large ε in the upper thermocline which they interpreted was likely generated by internal waves. Based on seismic oceanographic techniques, Gunn et al. (2021) also found dissipation rates between 10^{-5}-10^{-4} W kg^{-1} at about 100 m in the BMC, which is the shallower portion of the water column that they could resolve.

5.3. *Turbulent patches in the permanent pycnocline*

For the stations 19 and 21, located on the continental slope,

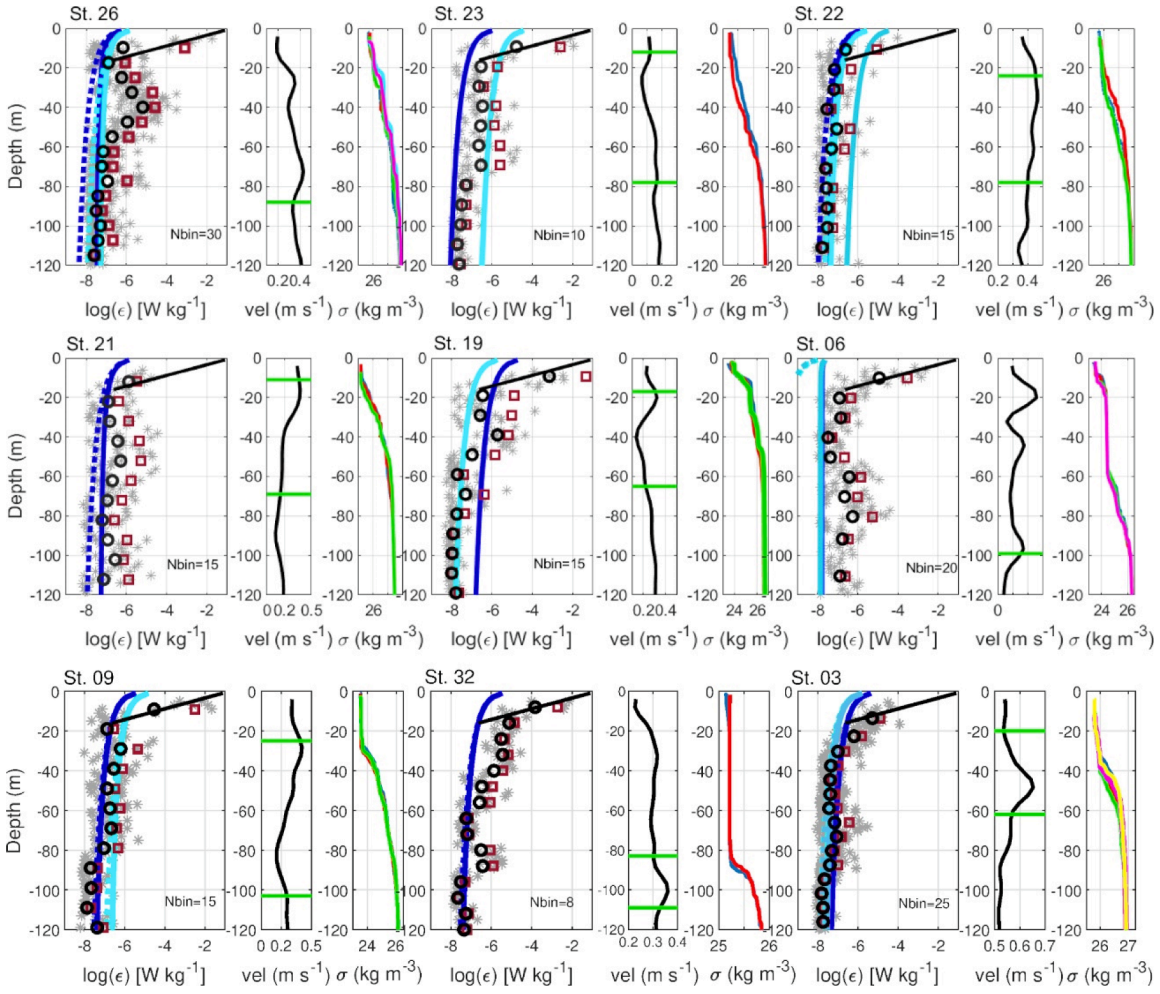

Fig. 17. Dissipation rates obtained for 2-m segments within the upper 120 m for all casts at stations 26, 23, 22, 21, 19, 06, 09, 32 and 03 (grey stars). The bin-average values are shown with brown squares (arithmetic mean) and black circles (geometric mean). The number of data points per bin is indicated. For each station, the velocity measured with the LADCP and the density profiles measured during the microstructure casts are presented in the right panels. The dissipation-rate curves are $\varepsilon(z) = 0.184e^{-0.85z}$ for z ≥ -18 m (black line), and $\varepsilon(z) = 1.5u_s^2/(kz)$ (blue dot-line) and $\varepsilon(z) = 1.5u_s^2/(kz) + 0.8J_B$ (blue solid-line) for z < -18 m; different shades of blue correspond to different meteorological forcing measured 1 h apart during measurements. The horizontal green lines in the velocity panels indicate the upper (when it exists) and lower limits of the seasonal pycnocline.

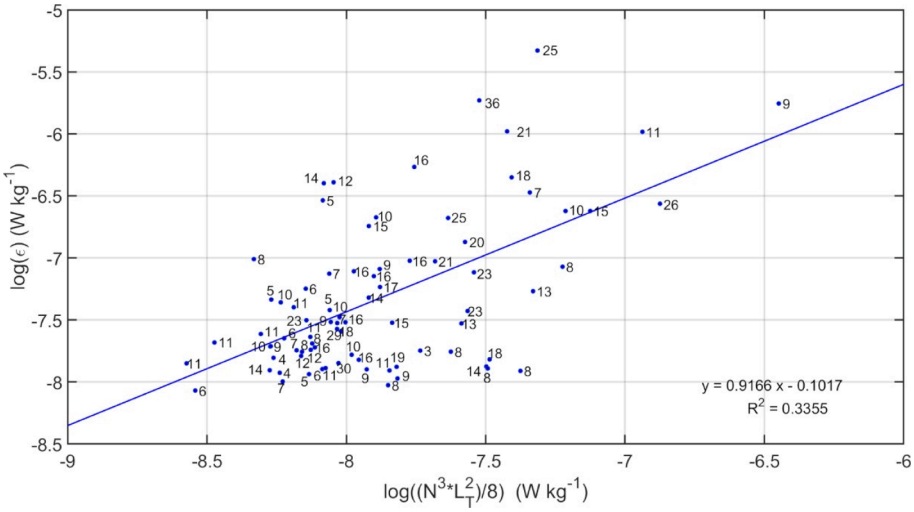

Fig. 18. Rate of transformation of available potential energy (APE) plotted as a function of dissipation rates for all the turbulent patches in stations 19 and 21, over the continental slope. The numbers indicate the thickness in meters of the patches.

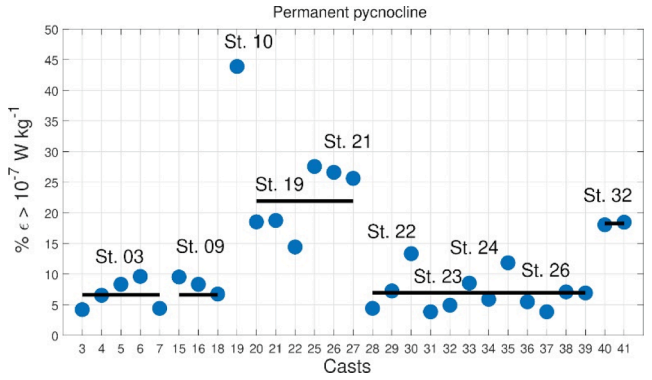

Fig. 19. Percentage of the water column in the permanent pycnocline where $\varepsilon > 10^{-7}\,\mathrm{W\,kg^{-1}}$, considering all different casts; the horizontal black lines indicate the mean value for the corresponding stations.

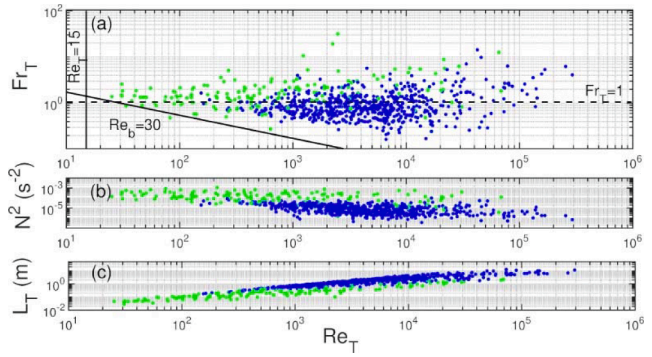

Fig. 20. (a) Hydrodynamic diagram of 2-m segments within the seasonal thermocline (in green) and the permanent thermocline (in blue) of all the casts recorded on stations 19 and 21. (b) Brunt-Väisälä frequency and (c) Thorpe scale for the same segments.

patches>3.5 m in the permanent pycnocline (below 70 m) have been identified through the method of the accumulative Thorpe displacement (section 3.3); recall that these are the only two stations where we have been able to apply this method. In total there are 80 patches ranging up to 36 m with mean dissipations from 8.5×10^{-9} to 4.7×10^{-6} W kg^{-1}.

In Fig. 18 the expected rate of APE to TKE transformation, $N^3L_T^2/8$, has been represented as a function of the dissipation rate, ε (section 3.3). The straight-line fit would represent that the APE release from shear instabilities is balanced by the dissipation rate. During each cast different stages of the mixing events are sampled, but the curve regression gives an integrated result. The lineal fit between $N^3L_T^2/8$ and ε, in logarithmic scale, indeed has a slope close to 1 ($R^2 = 0.33$), supporting the idea of the predominant local balance between production and dissipation in the permanent thermocline as it would be the case for small-scale shear instabilities. The relatively large scatter suggests other mechanism like internal waves (Palmer et al., 2015).

The entire set of patches in Fig. 18 covers 1025 m out of a total of 1572 m in the permanent pycnocline, so that patches represent 65 % of the water column, with patches thicker than 3.5 m occupying 19 % of the total sampled depth. In 23 % of the patches the dissipation rate is higher than 10^{-7} W kg^{-1}. This patch analysis has been done only for stations on the continental slope where L_T could be computed. Alternatively, the percentage of the water column in the permanent pycnocline where $\varepsilon > 10^{-7}\mathrm{W\,kg^{-1}}$ has been calculated for all the stations based on the mean dissipation rates within segments of 2 m (Fig. 19). For the casts in stations 19 (P20-*P*21) and 21 (P25-P27), these percentages are approximately 15 % and 27 %, respectively, consistent with the results based on the patch analyses. The mean percentage at these continental slope stations is about three times larger than in other stations, except for stations 10 and 32 that were sampled under relatively high-wind conditions (Table 2).

5.4. *The state of the turbulence*

Considering all casts in all stations, about 95 % of the 2-m segments fulfil the condition $Re_b > 30$, so turbulence can indeed be considered active. Complementary to this, for those stations where the Thorpe scale can be computed (19 and 21), the $Fr_T$and Re_Tnumbers have been

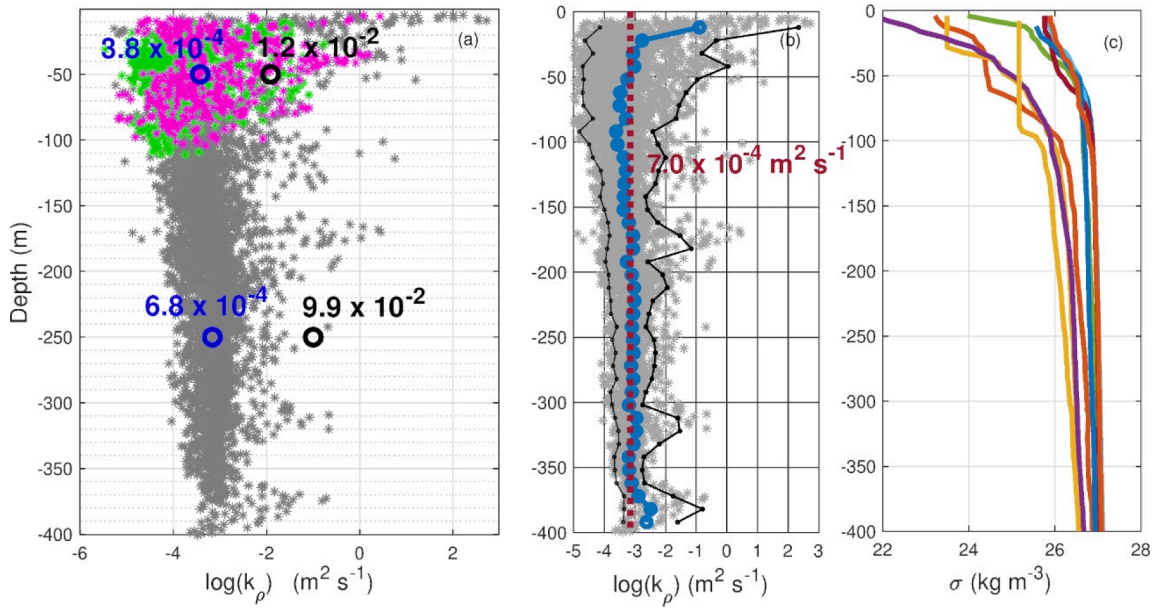

Fig. 21. (a) Diapycnal eddy diffusivities computed in 2-m segments for all casts. The empty circles stand for the geometrical (blue) and arithmetic (black) means for all segments in the seasonal and permanent pycnocline, respectively. The coloured symbols indicate the segments located within the seasonal pycnocline: green when the mixed layer is deeper than 10 m and magenta when shallower. (b) Geometrical mean diffusivities every 10 m and the corresponding 5 and 95 percentiles. The vertical line stands for the geometrical mean of all segments from the sea surface down to 400 m. (c) Density profiles of representative stations in this study.

calculated for 2-m segments and represented in the hydrodynamic diagram (Fig. 20). In Fig. 20a we present the lines $Fr_T = 15$ and $Re_b = 30$, which correspond to values where the turbulence is considered to decay (sections 3.7 and 3.8). The data points show that the turbulence remains active at all depths, with $Re_T > 15$ stretching over about 5 orders of magnitude. In Fig. 20b and 20c, both $N^2$and L_T are represented as a function of Re_T. N^2 is plotted to evaluate whether large Re_T are biased toward weak stratification. At the seasonal and permanent pycnoclines L_T increases with Re_T, but the largest L_T are observed in the permanent pycnocline, with relatively low stratification and high Re_T. The arithmetic mean of Fr_T is 1.6 and the geometric mean 1.1 (2.3/1.6 in the seasonal pycnocline and 1.4/1.0 in the permanent pycnocline). As already commented, it is expected that $Fr_T \cong 1$ at the time of maximum turbulent intensity.

6. Vertical mixing

6.1. Mean diapycnal eddy diffusivities

The diapycnal turbulent buoyancy flux is calculated as $J_b = -K_\rho N^2$, where K_ρ is the diapycnal eddy diffusivity of mass and N^2 the environment stratification. Following Osborn (1980), who assumed a local balance between $\varepsilon$and the production of TKE energy from the mean shear P and the buoyancy flux B, the diapycnal eddy diffusivity becomes $K_\rho = \gamma \frac{\varepsilon}{N^2}$, where $\gamma = \frac{Ri_f}{1-Ri_f}$ is the mixing coefficient. Setting the Richardson flux number or mixing efficiency, $Ri_f = B/P = 0.15$ leads to.$\gamma = 0.2$

There is a vast bibliography where Ri_f is parameterized with different variables describing the relative importance of the stratification with respect to the shear and the intensity of the turbulence, like Ri and Re_b, (Phillips, 1972; Gibson 1980; Lozovatsky et al., 2006) and even on the time life of the event (Pelegrí and Sangrà, 1998; Smyth, 2001). Caulfield (2021) argued that, in general, a flow is characterized by four non-dimensional parameters, but Gregg et al. (2018) recall that tracer experiments confirm that $\gamma = 0.2$ over a 30-fold range of diapycnal diffusivities. Accordingly results presented here have been computed following $K_\rho = 0.2\varepsilon/N^2$ (section 3.9).

The diffusivities calculated during the campaign are presented in Fig. 21a. Diffusivities span five orders of magnitude, even in the permanent pycnocline, and their variability is also very high with depth, mirroring the regions with the high dissipation rates.

The data recorded during 12 days in 11 stations (41 casts) in the frontal region of the encountering of subtropical and subantarctic waters should provide a robust statistic value of the regional diapycnal diffusivity. However, given the large range of variability, the extreme values dominate and the arithmetic mean is not a good representative of the measured values (Fig. 21a). Wells and Wells (1921) faced similar problem when studding the population of bacteria that present high spatial and temporal variability and introduced the geometric mean to better describe the size of the population and its evolution. The arithmetic mean considers the set of events as independent and the geometric mean considers them as sequential, hence addressing the combined effect of mixing events on the total fluxes. As stated by Wells and Wells (1921), when the variability is low, the geometric mean is slightly smaller but remains close to the arithmetic mean. However, the geometric mean is less sensitive to extreme values and, for situations of high variability, gives values that are more representative of the measurements than the arithmetic mean (Fig. 21a).

By introducing the geometric mean we have an objective method to compare different frontal locations and different layers. In Fig. 21b, the geometric mean for segments of 10 m is presented together with the percentiles 5 and 95. A coherent background vertical structure is observed with maximum values in the surface layers, minimum values in the seasonal thermocline extending roughly down to 150 m, and intermediate values in the permanent pycnocline – although with high individual diffusivities. Gunn et al. (2021) found the highest mixing rates at about 200 m, associated with submesoscale features about 30–40 km long. Orúe-Echevarría et al. (2019), based on the vertical correlation analysis of high-resolution SeaSoar measurements undertaken during the same campaign, found intrusions about 10–50 m thick and 10–20 km long.

Table 4
Geometric means of the diffusivities.

Stations	K_ρ (10^{-4} m^2 s^{-1})		
	Seasonal pycnocline	Permanent pycnocline	Entire water column
All	3.8	6.8	7.0
North of the front (09, 10, 06)	2.4	3.7	3.9
Upstream along the BC (32)	1.3	4.2	13.2
South of the front (22, 23, 24, 26)	5.9	7.5	7.4
Over the continental slope (19, 21)	3.8	8.8	8.3
Along MC (03)	1.8	7.0	6.2

The arithmetic mean of the seasonal-pycnocline diffusivity for all stations is $K_\rho = 1.2 \times 10^{-2}$m^2 s^{-1} and the geometric mean is $K_\rho = 3.8 \times 10^{-4}$m^2 s^{-1}. For the permanent pycnocline, the arithmetic mean is $K_\rho = 9.9 \times 10^{-2}$m^2 s^{-1} and the geometric mean is $K_\rho = 6.8 \times 10^{-4}$m^2 s^{-1}, about twice as in the seasonal pycnocline. The geometric mean for the entire column, including the upper mixed layer, is $K_\rho = 7.0 \times 10^{-4}$m^{2}s^{-1} (Table 4).

Overall, our data at the BMC show very high mixing rates in the upper 400 m of the water column, which are one or two orders of magnitude greater than the canonical value in the thermocline of 10^{-5}m^{2}s^{-1}, which makes sense considering that the BMC is among the most energetic regions in the world ocean (Chelton et al., 1990). The quantitative and qualitative results found in this study are in agreement with those obtained from seismic data in the BMC by Gunn et al. (2021). These authors hypothesize that the elevated mean mixing rates result from the proximity to the continental slope and the intense open-ocean dynamics.

6.2. Eddy diffusivities in different frontal areas

When exploring the mixing activity in different areas, the number of casts is substantially reduced but yet the geometric mean for the seasonal and permanent pycnocline provides consistent information. In Fig. 22 and Table 4, the results are compiled after dividing the BMC in areas north and south of the front, on the continental slope and over the paths of the BC (station 03) and MC (station 32).

In general, the mean diffusivity for the entire water column is similar to the mean diffusivity of the permanent pycnocline. The mean diffusivities in both the seasonal and permanent pycnoclines for those stations located south of the front (Fig. 22b, c, e) are about double than those located to the north (Fig. 22a, d). It is possible that the higher stratification and weaker currents of the BC as compared with the MC is the cause for this difference. The mean diffusivities in those stations over the slope are the largest and also present the highest variability (Fig. 22c). As has been commented before, the water masses of these stations are essentially the same as in those stations to the south of the front.

6.3. Driving mechanisms at the dissipative scales

In order to explore the driving dissipative mechanisms, we examine the distribution of the Turner angles and the Richardson numbers together with the turbulent kinetic energy dissipation rates – and the background temperature,T, salinity, S and sigma-theta, σ – for individ-

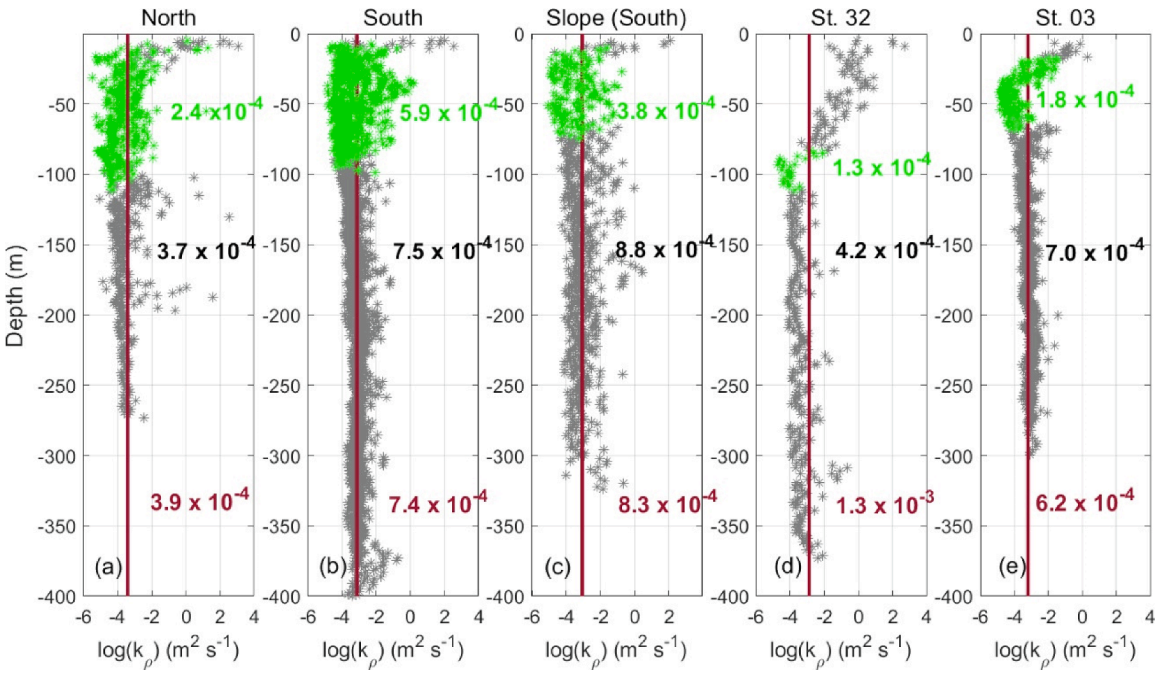

Fig. 22. Geometric mean of the diapycnal diffusivities in the seasonal (green) and permanent (grey) pycnoclines for clusters of stations grouped according to their relative position with respect to the front: (a) northern side, (b) southern side, (c) over the continental slope, and (d) far upstream along the BC (station 32) and (e) far upstream along the MC (station 03). Vertical lines stand for the geometric mean for the entire water column.

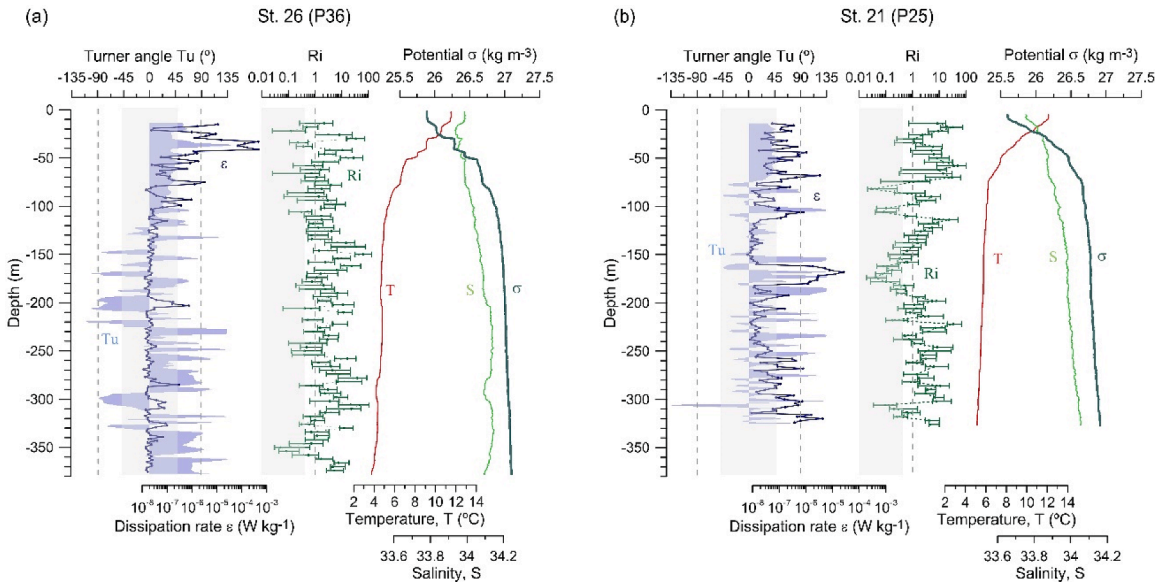

Fig. 23. Turner angles, turbulent kinetic energy dissipation rates and Richardson numbers as a function of depth for (a) cast P36 in station 26 and (b) cast P25 in station 21; for Ri, the interquartile range is represented. The corresponding temperature, salinity and potential density profiles are also presented.

ual casts. The Turner angle *Tu* tells us if specific segments are gravitationally stable (-45°< *Tu* < 45°), unstable (*Tu* > 90° or *Tu* < − 90°), or may experience salt fingering (SF, 45°< *Tu* < 90°) or double diffusion convection (DDC, − 90° < *Tu* < − 45°). A similar approach has been used by Zhu et al. (2021) in the Sub-Arctic Front. The Turner angle values are obtained from 1-cm microstructure data, which is low-pass filtered to 4 m and interpolated every 0.5 m (section 3.10). The gradient Richardson *Ri* values are also calculated every 4-m, using the 4-m LADCP velocity data and the 4-m median value for the squared buoyancy frequency N^2as obtained from the microstructure profiles. The whole set of N^2values combined with a unique value of the square of the vertical shear, S^2, has been used to determine the interquartile range (*IQR*) for *Ri* within the 4-m segment. Fig. 23 shows these variables for casts P36 (station 26) and P25 (station 21).

Station 26 (Fig. 23a) is a deep station located at the southern site of the front where subduction is very important (Fig. 2c). As commented, this is a highly dynamic region with the presence of strong currents, associated with fronts and mesoscale structures, such as eddies and filaments, which originate multiple intrusions at different levels in the water column and submesoscale structures are identified at all depths. At this station an intrusion of fresher water is observed extending from about 10 to 50 m depth coinciding with a layered structure on the temperature and sigma profiles. At these depths the *Ri* values are close to 0.25 for some segments and the lower limits of the *IQR* are below 0.25 in

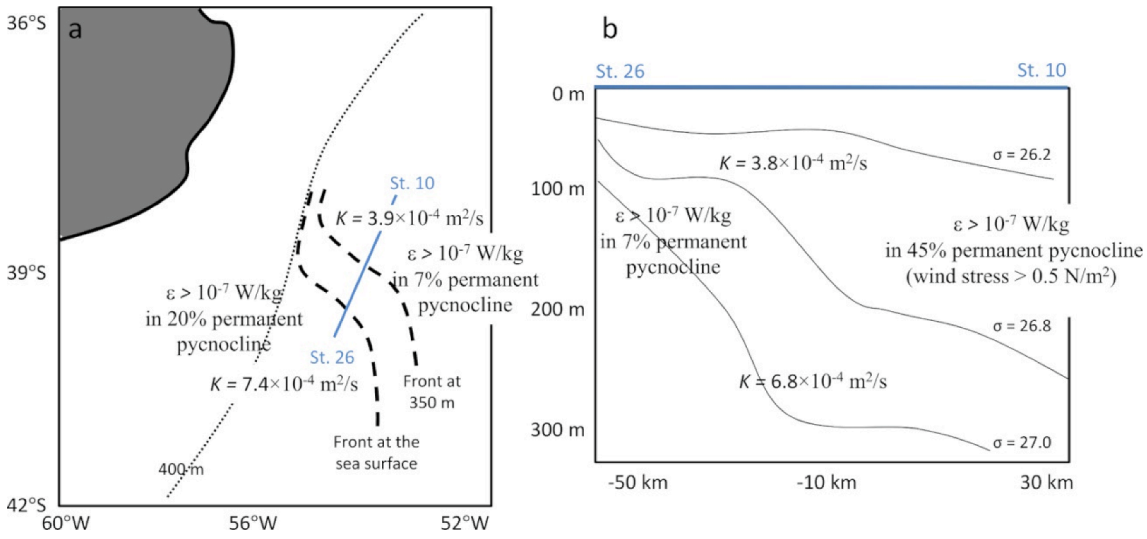

Fig. 24. Schematics with some major features of the spatial distribution of the TKE dissipation rates ε and the diapycnal eddy diffusivities *K* in the BMC frontal region. (a) Horizontal distribution of the (surface to 350 m) depth-averaged ε and *K* values. The dotted curve shows the position of the continental shelf break and the dashed curves the position of the front at the sea surface and at 350 m; the blue line illustrates a cross-frontal section that runs approximately between stations 26 and 10. (b) Vertical distribution along this cross-frontal section, illustrating the potential density (σ) distribution together with the near-surface and permanent thermocline *K* values and the percentage of the water column with ε values above 10^{-7} W kg^{-1} on both sides of the front.

most cases. These values indicate favourable conditions for vertical overturns caused by shear instabilities, probably generating K-H billows. Development of K-H instability is consistent with values of $Tu > 90°$, which indicates gravitational instability, coinciding with the step structure of the density profile. At the upper and lower parts of this highly dissipative region, the conditions are slightly favourable for salt fingers formation (Tu > 45°). Further, the high dissipation rates around 300 m depth coincide with a colder and fresher water intrusion with a thickness of about 20 m. In this case, *Ri* values are slightly larger and the *Tu* angle indicates double diffusive convection, a possible source of the high dissipation rates. Similar phenomenology is observed at about 200 m depth.

Station 21 (Fig. 23b) is a shallow station (547 m depth) with a mixed layer between 150 and 200 m (Fig. 6b). The values of *Ri* are below 1 within these depths, with the lowest values (<0.25) coinciding with the highest dissipation rates in a layer extending between 160 and 180 m. K-H instabilities due to internal waves breaking induced by the bathymetry could explain this event (Matsuno et al., 2005; Seim and Fer, 2011). The fact that high dissipation rates are not observed throughout the entire mixed layer, from 150 m to 200 m depth, could be interpreted as indicative of secondary instabilities occurring after primary K-H billowing (Smyth and Moum, 2012). This appears to be corroborated by the *Tu* angles, with stable layers where $-45° < Tu < 45°$ alternating with other layers where $Tu > 90°$ confirms gravitational instability. At both sides of this high energetic core, the *Tu* angles also denote gravitational unstable conditions.

The uncovering of the mechanisms that drive diapycnal mixing in the BMC deserves a wide and deep analysis, which falls beyond the original aim of this article. However, the examples presented here show that K-H instabilities are important mechanisms that drive mixing. Further, our results suggest that double-diffusion convection and salt fingering may also have a relevant role, although their relative importance has not yet been determined. Whether double diffusion regimes can actually occur without being disrupted by the mechanical turbulence, are still unclear (Nagai et al., 2021).

7. Conclusions

During the cruise, turbulence has been found to be very energetic in all BMC stations, exceeding $Re_T = 15$ and $Re_b = 30$. The arithmetic mean of Fr_T is 1.6 and the geometric mean 1.1. In the permanent pycnocline, most stations exhibit high-dissipation patches with vertical extensions ranging from several metres to about 30 m. Over the slope, $\varepsilon > 10^{-7}$W kg^{-1} in about 20 % of the 2-m segments, and for the remaining stations, $\varepsilon > 10^{-7}$W kg^{-1}in about 7 % of these segments. In stations 10 and 32, where weather conditions were fairly rough, the percentages are higher.

In the upper 120 m, the modified law of the wall (considering the buoyancy flux, $\varepsilon_{wall} + 0.8J_b$) fits the background dissipations well, but in all stations there are segments with dissipation rates up two orders of magnitude higher (up to 10^{-5}Wkg^{-1}). High dissipation rates within these upper layers coincide with high vertical shear, possibly related to the convergence of the two currents or to the generation of internal waves by the submesoscalar features. Remarkable layered structures are observed, which appear related to intruding filaments generated at the front.

Below the mixed layer, active turbulence appears mostly related to small-scale shear-driven instabilities, as shown by the low *Ri* numbers. In those stations over the continental slope, our data is consistent with near-bottom mixing resulting from the breaking of internal waves. In the thermocline layers, there are thermohaline intrusions that create inversions in the temperature and salinity profiles, leading to double diffusive convection (DDC) and salt fingering (SF), with high-dissipation layers. The relative intensity and effect of both DDC and SF on the diapycnal fluxes remains yet to be determined.

As a result of the high variability and large range of K_ρ values, which greatly mirror the ε distribution, the arithmetic mean is largely dominated by extreme values. In contrast, the geometric which is less sensitive to extreme values and is a good estimate of the most likely value. The geometric mean of the diffusivities in the seasonal pycnocline is 3.8×10^{-4}m^2 s^{-1}, while in the permanent pycnocline this mean reaches 6.8×10^{-4}m^2 s^{-1}. The geometric mean for the entire water column (from the sea surface down to about 400 m) is $K_\rho = 7.0 \times 10^{-4}$m^{2}s^{-1}. These values are considerably greater than the canonical value in the thermocline of 10^{-5}m^{2}s^{-1}.

The geometric mean values of $K_\rho$in the more homogeneous and energetic waters to the south of the front (7.4×10^{-4}m^{2}s^{-1}) are about twice those in the more stratified and slower waters to the north (3.9×10^{-4}m^{2}s^{-1}). It seems likely that the higher stratification and weaker

vertical shear of the BC as compared with the MC is the cause for this difference.

Our results have shown that vertical diffusivity and diapycnal fluxes are largely enhanced in an intense frontal system such as the Brazil-Malvinas Confluence (Fig. 24). This is of special relevance as frontal systems are often imagined as barriers between different water masses, as actual frontiers between subpolar, subtropical and tropical regions. However, intense vertical mixing in frontal systems, which often accompanies the unstable mesoscale and submesoscale frontal features, may prove that fronts are indeed highly energetic regions that sustain the worldwide vertical transfer of key properties such as heat and nutrients.

Declaration of Competing Interest

The authors declare that they have no known competing financial interests or personal relationships that could have appeared to influence the work reported in this paper.

Data availability

Data will be made available on request.

Acknowledgements

We are very grateful to the crew of R/V Hespérides for his support during the RETRO-BMC cruise. This study has been supported by the Spanish Government through projects VA-DE-RETRO (CTM2014-56987-P) and SAGA (RTI2018-100844-B-C33).

References

Alford, M.H., 2001. Internal swell generation: The spatial distribution of energy flux from the wind to mixed layer near-inertial modes. J. Phys. Oceanogr. 31 (8), 2359–2368. https://doi.org/10.1175/1520-0485(2001)031<2359:ISGTSD>2.0.CO;2.

Annis, A., Moum, J.N., 1995. Surface wave-turbulence interactions: scaling epsilon near the sea surface. J. Phys. Oceanogr. 25 (9), 2025–2045. https://doi.org/10.1175/15200485(1995)025<2025:SWISNT>2.0.CO;2.

Arcos-Pulido, M., Rodríguez-Santana, A., Emelianov, M., Paka, V., Arístegui, J., Benavides, M., Sangra, P., Machin, F., Garcia-Weil, L., Estrada-Allis, S., 2014. Diapycnal nutrient fluxes on the northern boundary of Cape Ghir upwelling region. Deep. Res. Part I: Oceanogr. Res. Pap. 84, 100–109. https://doi.org/10.1016/j.dsr.2013.10.010.

Bastida, I., Planella, J., Roget, E., Guillén, J., Puig, P., Sánchez, X., 2012. Dinámica de mezcla en la plataforma continental del Ebro. Sci. Mar. 76 (suppl.1), 31–43.

Berden, G., Charo, M., Mooler, O.O., Pola, A.R., 2020. Circulation and Hydrography in the Western South Atlantic Shelf and Export to the Deep Adjacent Ocean: 30 degrees S to 40 degrees S.. J. Geophys. Res. Oceans, 125(10), e2020JC016500. 10.1029/2020JC016500.

Canuto, V.M., Cheng, Y., 2020. Sub-mesoscales at ocean fronts: dissipation if eddy kinematic energy. J. Geophys. Res. Oceans. 125 (12), 8p. https://doi.org/10.1029/2020JC016252.

Carpenter, J.R., Rodrigues, A., Schultze, L.K.P., Merckelbach, L.M., Suzuki, N., Baschek, B., Umlauf, L., 2020. Shear Instability and Turbulence Within a Submesoscale Front Following a Storm. Geophys. Res. Lett. 47 (23), 20GL090365. https://doi.org/10.1029/2020GL090365.

Caulfield, C.P., 2021. Layering, Instabilities, and Mixing in Turbulent Stratified Flows. Annu. Rev. Fluid Mech. 53, 113–145. https://www.annualreviews.org/doi/10.1146/annurev-fluid-042320-100458.

Chelton, D.B., Schlax, M.G., Witter, D. L., Richman, J., 1990. Geosat altimeter observations of the surface circulation of the southern ocean, J. Geophys. Res., 95, 17.877–17.903. 10.1029/JC095iC10p17877.

Crawford, W.R., 1986. A comparison of length scales and decay times of turbulence in stably stratified flows. J. Phys. Oceanogr. 16 (11), 1847–1854. https://doi.org/10.1175/1520-0485(1986)016<1847:ACOLSA>2.0.CO;2.

Cui, Y.S., Wu, J.X., Qui, C.H., 2018. Enhanced mixing by patchy turbulence in the northern South China Sea. Cont. Shelf Res. 166, 34–43. https://doi.org/10.1016/j.csr.2018.06.013.

D'Asaro, E:, Lee, C, Rainville, L., Harcourt,,R., Thomas, L., 2011. Enhanced turbulence and energy dissipation at ocean fronts. Science, 332(6027), 318–2. 10.1126/science.1201515.

Dillon, T.M., 1982. Vertical overturns: a comparison of Thorpe and Ozmidov length scales. J. Geophys. Res. 87, 9601–9613. https://doi.org/10.1029/JC087iC12p09601.

Egbert, G., Ray, R., 2000. Significant dissipation of tidal energy in the deep ocean inferred from satellite altimeter data. Nature 405, 775–778. https://doi.org/10.1038/35015531.

Ferron, B., Mercier, H., Speer, K., Gargett, A., Polzin, K., 1998. Mixing in the Romanche fracture zone. J. Phys. Oceanogr. 28, 1929–1945. https://doi.org/10.1175/1520-0485(1998)028<1929:MITRFZ>2.0.CO;2.

Ferron, B., Bouruet-Aubertot, P., Schroeder, K., Bryden, H.L., Cuypers, Y., Borghini, M., 2021. Contribution of Thermohaline Staircases to Deep Water Mass Modifications in the Western Mediterranean Sea From Microstructure Observations. Front. Mar. Sci. 8, 664509 https://doi.org/10.3389/fmars.2021.664509.

Franco, B.C., Palma, E.D:, Combes, V., Acha, E.M., Saraceno, M., 2018. Modeling the Offshore Export of Subantarctic Shelf Waters From the Patagonian Shelf. J. Geophys. Res. Oceans,123(7), 4491-4502. 10.1029/2018JC013824.

GEBCO (General Bathymetric Chart of the Oceans). (2008). GEBCO_08 Grid, version 20100927. http://www.gebco.net.

Geyer, W.R., Lavery, A.C., Scully, M.E., Trowbridge, J.H., J.h., 2010. Mixing by shear instability at high Reynolds number. Geophys. Res. Lett. 37, L22607. https://doi.org/10.1029/2010GL045272.

Gibson, C.H., 1980. Fossil temperature, salinity and vorticity turbulence in the ocean. In: Nihoul, J.C.J. (Ed.), Marine Turbulence. Elsevier, Amsterdam, pp. 221–257.

Gibson, C.H., 1991. Laboratory, numerical, and oceanic fossil turbulence in rotating and stratified flow. J. Geophys. Res. 96, 12549–12566. https://doi.org/10.1029/91JC00186.

Gnanadesikan, A., Slater, R.D., Gruber, N., Sarmiento, J.L., 2002. Oceanic vertical exchange and new production: a comparison between models and observations. Deep-Sea Research II 49, 363–401. https://doi.org/10.1016/S0967-0645(01)00107-2.

Goni, G.J., Bringas, F., Dinezio, P., N., 2011. Observed low frequency variability of the Brazil Current front. J. Geophys. Res. Oceans 116 (10), C10037. https://doi.org/10.1029/2011JC007198.

Gordon, A.L., 1989. Brazil-Malvinas Confluence – 1984. Deep-Sea Res. Pt I 36 (3), 359–384. https://doi.org/10.1016/0198-0149(89)90042-3.

Gregg, M.C., Winkel, D.P., Sanford, T.B., Peters, H., 1996. Turbulence produced by internal waves in the oceanic thermocline at mid and low latitudes. Dynam. Atmos. Oceans 24, 1–14. https://doi.org/10.1016/0377-0265(95)00406-8.

Gregg, M.C., D'Asaro, E.A., Riley, J.J., Kunze, E., 2018. Mixing efficiency in the ocean. Ann. Rev. Mar. Sci. 10, 443–473. https://doi.org/10.1146/annurev-marine-121916-063643.

Gunn, K.L., Dickinson, A., White, N.J., Caulfield, C.P., 2021. Vertical Mixing and Heat Fluxes Conditioned by a Seismically Imaged Oceanic Front. Front. Mar. Sci. 8, 1–17. https://doi.org/10.3389/fmars.2021.697179.

Hamilton, J.M., Lewis, M.R., Ruddick, B.R., 1989. Vertical fluxes of nitrate associated with salt fingers in the world's oceans. J. Geophys. Res. 94 (C2), 2137–2145. https://doi.org/10.1029/JC094iC02p02137.

Han, I.-S., Kamio, K., Matsuno, T., Manda, I., A., 2001. High frequency current fluctuations and cross shelf flows around the pycnocline near the shelf break in the East China Sea. J. Oceanogr. 57, 235–249. https://doi.org/10.1023/A:1011199325842.

Imberger, J., Ivey, G.N., 1991. On the nature of turbulence in a stratified fluid. 2. Application to lakes. J. Phys. Oceanogr. 21 (5), 659–680. https://doi.org/10.1175/1520-0485(1991)021<0659:OTNOTI>2.0.CO;2.

Inall, M.E., Toberman, M., Polton, J.A., Palmer, M.R., Green, J.A.M., Rippeth, T.P., 2021. Shelf Seas Baroclinic Energy Loss: Pycnocline Mixing and Bottom Boundary Layer Dissipation. J. Geophys. Res. Oceans 126 (8), 1–22. https://doi.org/10.1029/2020JC016528.

Ivey, G.N., Imberger, J., 1991. On the nature of turbulence in a stratified fluid. Part II: The energetics of mixing. J Physical Oceanography 21, 650–658. https://doi.org/10.1175/1520-0485(1991)021<0650:OTNOTI>2.0.CO;2.

Ivey, G.N., Nokes, R.I., 1989. Vertical mixing due to breaking of critical waves on sloping boundaries. J. Fluid Mech. 204, 479–500. https://doi.org/10.1017/S0022112089001849.

Jing., Z., Wu, L., 2010. Seasonal variation of turbulent diapycnal mixing in the northwestern Pacific stirred by wind stress. Geophysy. Res. Lett. 37, L23604. 10.1029/2010GL045418.

Johnston, T.M.S., Rudnick, D.L., Pallàs-Sanz, E., 2011. Elevated mixing at a front. J. Geophys. Res. 116, C11033. https://doi.org/10.1029/2011JC007192.

Jullion, L., Heywood, K.J., Naveira Garabato, A,C., Stevens, D.P., 2010. Circulation and water mass modification in the Brazil-Malvinas Confluence. J. Phys. Oceanogr. 40 (5), 845–864. 10.1175/2009JPO4174.1.

Kantha, L., Clayson, C., 2000. Small scale processes in Geophysical Flows. International Geophysics Series, Vol. 67. Academic Press. ISBN: 9780124340701; eBook ISBN: 9780080517292.

Koenig, Z., Fer, I., Kolås, E., Fossum, T.O., Norgren, P., Ludvigsen, M., 2020. Observations of Turbulence at a Near-SurfaceTemperature Front in the Arctic Ocean. J. Geophys. Res. 20, pp. https://doi.org/10.1029/2019JC015526.

Legeckis, R., Gordon, A. L., 1982. Satellite observations of the Brazil and Falkland currents 1975, 1976, and 1978. Deep Sea Res. Part I, Oceanogr. Res. Pap. 29(3), 375–401.10.1016/0198-0149(82)90101-7.

Lengfeld, K., Macke, A., Feister, U., Uldner, U., 2010. Parameterization of solar radiation from model and observations. Meteorologische Zeitschrift. 19, 25–33. https://doi.org/10.1127/0941-2948/2010/0423.

Lentini, C.A.D., Goni, G.J., Olson, D.B., 2006. Investigation of Brazil current rings in the confluence region. J. Geophys. Res. Oceans 111 (6). https://doi.org/10.1029/2005JC002988.

Lozovatsky, I., Figueroa, M., Roget, E., Fernando, H.J.S., Shapovalov, S., 2005. Observations and scaling of the upper mixed layer in the North Atlantic. J. Geophys. Res. 110 (C5), C05013. https://doi.org/10.1029/2004JC002708.
Lozovatsky, I., Roget, E., Fernando, H., Figueroa, M., Shapovalov, S., 2006. Sheared turbulence in a weakly stratified upper ocean. Deep Sea Res. Part I. Oceanogr. Res. Pap. 53, 387–407. https://doi.org/10.1016/j.dsr.2005.10.002.
Lueck, R.G., Picklo, J.J., 1990. Thermal inertia of conductivity cells: Observations with a Sea-Bird Cell. J. Atmos. Oceanic Technol. 7, 756–768. https://doi.org/10.1175/1520-0426(1990)007<0756:TIOCCO>2.0.CO;2.
Ma, Y.C., Peltier, W.R., 2021. Parametrization of irreversible diapycnal diffusivity in salt-fingering turbulence using DNS. J. Fluid Mech. 911, A9. https://doi.org/10.1017/jfm.2020.1018.
Mack, S.A., 1985. Two-Dimensional Measurements of Ocean Microstructure: The Role of Double Diffusion. J. Phys. Oceanogr. 15 (11), 1581–1604. https://doi.org/10.1175/1520-0485(1985)015<1581:TDMOOM>2.0.CO;2.
MacKinnon, J.A., Zhao, Z., Whalen, C.B., Waterhouse, A.F., Trossman, D.S., Sun, O.M., et al., 2017. Climate process team on internal wave-driven ocean mixing. Bull. Am. Meteorol. Soc. 98 (11), 2429–2454. https://doi.org/10.1175/BAMS-D-16-0030.1.
Maffioli, A., Brethouwer, G., Lindborg, E., 2016. Mixing efficiency in stratified turbulence. J. Fluid Mech. 794, R3. https://doi.org/10.1017/jfm.2016.206.
Mahadevan, A., 2016. The Impact of Submesoscale Physics on Primary Productivity of Plankton. Ann. Rev. Mar. Sci. 8, 161–184. https://doi.org/10.1146/annurev-marine-010814-015912.
Mahony, J.J., 1977. Kelvin-Helmholtz waves in the ocean? J. Fluid Mech. 82 (1), 1–16. https://doi.org/10.1017/s0022112077000500.
Mater, B.D., Venayagamoorthy, S.K., Laurent, L.S., Moum, J.N., 2015. Biases in thorpe-scale estimates of turbulence dissipation. Part I: Assessments from large-scale overturns in oceanographic data. J. Phys. Oceanogr. 45 (10), 2497–2521. https://doi.org/10.1175/JPO-D-14-0128.1.
Matsuno, T., Shimizu, M., Morri, Y., Nishida, H., Takai, Y., 2005. Measurments of the turbulent energy dissipation rate around the shelf break in the East China Sea. J. Oceanogr. 61, 1029–2005. https://doi.org/10.1007/s10872-006-0019-9.
Meyer, A., Sloyan, B.M., Polzin, K.L., Phillips, H.E., Bindoff, N.L., 2015. Mixing Variability in the Southern Ocean. J. Phys. Oceanogr. 45 (4), 966–987. https://doi.org/10.1175/JPO-D-14-0110.1.
Miles, J., 1961. On the stability of heterogeneous shear flows. J. Fluid Mech. 10, 496–515. https://doi.org/10.1017/S0022112061000305.
Möller, O.O., Piola, A.R., Freitas, A.C., Campos, E.J.D, 2008. The effects of river discharge and seasonal winds on the shelf off southeastern South America. Cont. Shelf Res. 28(13), 1607–10.1016/j.csr.2008.03.012.
Morgan, P.P., 1994. SEAWATER. A library of MATLAB computational routines for the properties of sea water. CSIRO Marine Laboratories, Report 222, 29 pp.
Munk, W.H., 1966. Abyssal recipes. Deep-Sea Res. Oceanogr. Abstr. 13 (4), 707–730. https://doi.org/10.1016/0011-7471(66)90602-4.
Nagai, T., Tandon, A., Yamazaki, H., Doubell, M.J., Gallager, S., 2012. Direct observations of microscale turbulence and thermohaline structure in the Kuroshio Front. J. Geophys. Res. Oceans 117 (8), 1–21. https://doi.org/10.1029/2011JC007228.
Nagai, T., Quintana, G.M.R., Gomez, G.S.D., Hashihama, F., Komatsu, K., 2021. Elevated turbulent and double-diffusive nutrient flux in the Kuroshio over the Izu Ridge and in the Kuroshio Extension. J. Oceanogr. 77 (1), 55–74. https://doi.org/10.1007/s10872-020-00582-2.
Orsi, A.H., Johnson, G.C., Bullister, J.L., 1999. Circulation, mixing, and production of Antarctic Bottom Water. Prog. Oceanogr. 43 (1), 55–109. https://doi.org/10.1016/S0079-6611(99)00004-X.
Orúe-Echevarría, D., Pelegrí, J.L., Machínm, F., Hernández-Guerram, A., Emelianov, M., 2019a. Inverse modeling the Brazil-Malvinas Confluence. Journal of Geophysical Research: Oceans 124, 527–554. https://doi.org/10.1029/2018JC014733.
Orúe-Echevarría, D., Castellanos, P., Sans, J., Emelianov, M., Vallès-Casanova, I., Pelegrí, J.L., 2019b. Temperature Spatiotemporal Correlation Scales in the Brazil-Malvinas Confluence from High-Resolution In Situ and Remote Sensing Data. Geophys. Res. Lett. 46 (22), 13234–13243. https://doi.org/10.1029/2019GL084246.
Orúe-Echevarría D., Pelegrí, J.L., Alonso-González, I.J., Benítez-Barrios, V.M., Emelianov, M., García-Olivares, A., Gasser i Rubinat, De La Fuente, M.P., Herrero, C., Isern-Fontanet, J. Masdeu-Navarro, M., Peña-Izquierdo, J., Piola, A.R., Ramírez-Garrido, Rosell-Fieschi, M., Salvador, J., Saraceno, M., Valla, Vallès-Casanova, I., 2021. A view of the Brazil-Malvinas Confluence, March 2015. Deep-Sea Research I, 172, 103533.
Orúe-Echevarría, D., Pelegrí, J.L., Castellanos, P., Guallar, C., Marotta, H., Marrasé, C., Martín, J., Masdeu-Navarro, M., Paniagua, G.F., Peña-Izquierdo, J., Puigdefábregas, J., Rodríguez-Fonseca, B., Roget, E., Rosell-Fieschi, M., Salat, J., Salvador, J., Vallès-Casanova, I., Vidal, M., Viúdez, A., 2020. Dataset on the RETRO-BMC cruise onboard the R/V Hespérides, April 2017. Brazil-Malvinas Confluence. Data in Brief 30, 105412. https://doi.org/10.1016/j.dib.2020.105412.
Osborn, T.R., 1980. Estimates of local rate of vertical diffusion from dissipation measurements. J. Phys. Oceanogr. 10, 83–89. https://doi.org/10.1175/1520-0485(1980)010<0083:EOTLRO>2.0.CO;2.
Palmer, M.R., Stephenson, G.R., Inall, M.E., Balfour, C., DÚsterhus, A., Greem, J.A.M, 2015. Turulence and mixing by internal waves in the Celtic Sea determined from ocean glider microstructure measurements. J. Mar. Syst. 144, 57–69. 10.1016/j.jmarsys.2014.11.005.
Paniagua, G.F., Saraceno, M., Piola, A.R., Guerrero, R., Provost, C., Ferrari, R., Lago, L.S., Camila I. Artana, C.I., 2018. Malvinas Current at 40°S–41°S: First Assessment of Temperature and Salinity Temporal Variability. J. Geophys. Res. Oceans 123(8), 5323–5340.10.1029/2017JC013666.
Payne, R.E., 1972. Albedo of the sea Surface. J. Atmos. Sci. 29 (5), 959–970. https://doi.org/10.1175/1520-0469(1972)029<0959:AOTSS>2.0.CO;2.
Pelegrí, J.L., Marrero-Díaz, A., Ratsimandresey, A.W., 2006. Nutrient irrigation of the North Atlantic. Progr. Oceanogr. 70, 366–406. https://doi.org/10.1016/j.pocean.2006.03.018.
Pelegrí, J.L., Orúe-Echevarría, D., Castellanos, P., Guallar, C., Marotta, H., Marrasé, C., et al., 2019. The RETRO-BMC cruise onboard the R/V Hespérides, April 2017, Brazil-Malvinas Confluence: Hydrographic and drifters data. Digital CSIC. 10.20350/digitalCSIC/8951.
Pelegrí, J.L., Sangrà, P., 1998. A mechanism for layer formation in stratified geophysical flows. J. Geophys. Res. 103, 30679–30693. https://doi.org/10.1029/98JC01627.
Peters, H., Gregg, M.C., Sanford, T.B., 1995. On the parameterization of equatorial turbulence. Effect of fine scale variations bellow the range of the diurnal cycle. J. Geophys. Res. Oceans 100 (C9), 18333–18348. https://doi.org/10.1029/95JC01513.
Phillips, O.M., 1972. Turbulence in a strongly stratified fluid – is it unstable? Deep-Sea Res. Oceanogr. Abstr. 19 (1), 79–81. https://doi.org/10.1016/0011-7471(72)90074-5.
Phillips, O.M., Banner, M.L., 1974. Wave breaking in the presence of wind drift and swell. J. Fluid Mech. 66 (4), 625–640. https://doi.org/10.1017/S0022112074000413.
Piola, A.R., Gordon, A.L., 1989. Intermediate waters in the southest South Atlantic. Deep Sea Res. Part I Oceanogr. Res. Pap. 36(1), 1–16. 10.1016/0198-0149(89)90015-0.
Piola, A.R., Campos, E.J.D., Moller, O.O., Charo, M., Martinez, C., 2000. Subtropical Shelf Front off eastern South America. Geophys. Res. Oceans 105 (C3), 6565–6578. https://doi.org/10.1029/1999JC000300.
Planella Morato, J., Roget, E., Lozovatsky, I., 2011. Statistics of microstructure patchiness in a stratified lake. J. Geophys. Res. Oceans 116, C10035. https://doi.org/10.1029/2010JC006911.
Pollard, R., Tréguer, P., Read, J.F., 2006. Quantifying nutrient supply to the Southern Ocean. J. Geophys. Res. 111, C0501. https://doi.org/10.1029/2005JC003076.
Portwood, G. D., Kops, S. M. de Bruyn, ;Taylor, J. R., Salehipour, H., Caulfield, C.P. 2016. Robust identification of dynamically distinct regions in stratified turbulence J. Fluid Mech. 807, R2. 10.1017/jfm.2016.617.
Prandke, H., Holtsh, K., Stips, A., 2000. MITEC technology development: the microstructure-turbulence measuring system MSS. EUR 19733 EN. Ispra Joint Research Center, European Comission.
Price, J.F., Weller, R.A., Pinkel, R., 1986. Diurnal cycling – observations and models of the upper ocean response to diurnal heating, cooling, and wind mixing. J. Geophys. Res. 91 (C7), 8411–8427. https://doi.org/10.1029/JC091iC07p08411.
Roget, E., Lozovatsky, I., Sanchez, X., Figueroa, M., 2006. Microstructure measurements in natural waters: Methodology and applications. Prog. Oceanogr. 70(2–4), 126–148.10.1016/j.pocean.2006.07.003.
Roget, E., Lozovatsky, I., Sanchez, X., Figueroa, M., 2007. Corrigendum to Microstructure measurements in natural waters: Methodology and applications. Prog. Oceanogr. 72 (1), 114. https://doi.org/10.1016/j.pocean.2006.10.002.
Rohr, J.J., Itsweire, E.C., Van Atta, C.W., 1984. Mixing efficiency in stably stratified decaying turbulence. Geophys. Astrophys. Fluid Dyn. 29, 221–236. https://doi.org/10.1080/03091928408248190.
Ruddick, B., 1983. A practical indicator of the stability of the water column to double-diffusive activity. Deep-Sea Res. 30A, 1105–1107. https://doi.org/10.1016/0198-0149(83)90063-8.
Ruddick, B., Anis, A., Thomson, K., 2000. Maximum likelihood spectral fitting: the Batchelor spectrum. J Atmos Ocean Technol. 17, 1541–1555. https://doi.org/10.1175/1520-0426(2000)017<1541:MLSFTB>2.0.CO;2.
Sanchez, X., Roget, E., 2007. Microstructure measurements and heat flux calculations of a triple-diffusive process in a lake within the diffusive layer convection regime. J. Geophys. Res. Oceans 112 (C2), C02012. https://doi.org/10.1029/2006JC003750.
Seim, K.S., Fer, I., 2011. Mixing in the stratified interface of the Faroe Bank Channel overflow: The role of transverse circulation and internal waves. J. Geophys. Res. 2011 (116), C07022. https://doi.org/10.1029/2010JC006805.
Smyth, W.D., Moum, J.N., 2000. Length scales of turbulence in stably stratified mixing layers. Phys. Fluids 12 (6), 1327–1342. https://doi.org/10.1063/1.870385.
Smyth, W.D., Moum, J.N., 2012. Ocean Mixing by Kelvin-Helmholtz instability. Oceanography. 25 (2), 140–149. https://doi.org/10.5670/oceanog.2012.49.
Smyth, W.D., Moum, J.N., Caldwell, D.R., 2001. The efficiency of mixing in turbulent patches: Inferences from direct simulations and microstructure observations. J. Phys .Oceanogr..31(8 PART 1), 1969–92. 10.1175/1520-0485(2001)031<1969:TEOMIT>2.0.CO;2.
Sprintall, J., Cronin, M.F., 2011. Upper Ocean Vertical Structure. Encycl Ocean Sci. 3120–3128 https://doi.org/10.1006/rwos.2001.0149.
St Laurent, L., Schmitt, R.W., 1999. The contribution of salt fingers to vertical mixing in the North Atlantic Tracer Release Experiment. J Phys Oceanogr. 29 (7), 1404–1424. https://doi.org/10.1175/1520-0485(1999)029<1404:TCOSFT>2.0.CO;2.
St. Laurent, L., Simmons, H., 2006. Estimates of power consumed by mixing in the ocean interior. J. Clim. 19 (19), 4877-4890. 10.1175/JCLI3887.1.
Stevens, C.L., 2018. Turbulent length scales in a fast-flowing, weakly stratified, strait: Cook Strait. New Zealand. Ocean Sci. 14 (4), 801–812. https://doi.org/10.5194/os-14-801-2018.
Stramma, L., England, M., 1999. On the water masses and mean circulation of the South Atlantic Ocean. J. Geophys. Res. Ocean 104 (C9), 20863–20883. https://doi.org/10.1029/1999JC900139.
Stramma, L., Kieke, D., Rhein, M., Schott, F., Yashayaev, I., Koltermann, K.P., 2004. Deep water changes at the western boundary of the subpolar North Atlantic during 1996 to 2001. 51(8): 1033–1056. 10.1016/j.dsr.2004.04.001.

Strang, E.J., Fernando, H., 2001. Entrainment and mixing in stratified shear flows. J. Fluid Mech. 428, 349–386. https://doi.org/10.1017/S0022112000002706.
Sullivan, P.P., McWilliams, J.C., Patton, E.G., 2014. Large-Eddy Simulation of Marine Atmospheric Boundary Layers above a Spectrum of Moving Waves. J Atmos Sci. 71 (11), 4001–4027. https://doi.org/10.1175/JAS-D-14-0095.1.
Taylor, J.R., Zhou, Q., 2017. A multi-parameter criterion for layer formation in a stratified shear flow using sorted buoyancy coordinated. J. Fluid Mech. 823, R5. https://doi.org/10.1017/jfm.2017.375.
Thomas, L.N., Taylor, J.R., D'Asaro, E.A., Lee, C.M. Klymak, J.M., Shcherbina, A., 2016. Symmetric Instability, Inertial Oscillations, and Turbulence at the Gulf Stream Front. J. Phys. Oceanogr.46(1), 197-217. 10.1175/JPO-D-15-0008.1.
Thorpe, S.A., 1977. Turbulence and mixing in a Scottish loch. Philos. trans. R. Soc. Lond. A286, 125–181.
Thorpe, S. A., Liu, Z., 2009. Marginal Instability? J. Phys. Oceanogr. 39(9), 2373–2381.10.1175/2009JPO4153.1.
Turner, J.S., 1973. Buoyancy effects in fluids. University Press, Cambridge [Eng.].
Valla, D., Piola, A.R., Meinen, C.S., Campos, E., 2018. Strong Mixing and Recirculation in the Northwestern Argentine Basin. J. Geophys. Res. Oceans 123 (7), 4624–4648. https://doi.org/10.1029/2018JC013907.
Waterhouse, A.F., Mackinnon, J.A., Nash, J.D., Alford, M.H., Kunze, E., Simmons, H.L., et al., 2014. Global patterns of diapycnal mixing from measurements of the turbulent dissipation rate. J. Phys. Oceanogr. 44 (7), 1854–1872. https://doi.org/10.1175/JPO-D-13-0104.1.
Wells, P.V., Wells, W.F., 1921. On the dilution method of counting bacteria. J. Wash. Acad. Sci. 11 (12), 265–273. https://www.jstor.org/stable/24532592.
Wenegrat, J.O., Thomas, L.N., Sundermeyer, M.A., Taylor, J.R., D'Asaro, E.D., Klymak, J. M., Shearman, R.K., Lee, C.M., 2020. Enhanced mixing across the gyre boundary at the Gulf Stream front. Proc. Natl. Acad. Sci. U.S.A. 117 (30), 17607–17614. https://doi.org/10.1073/pnas.2005558117.
Wesson, J.C., Gregg, M.C., 1994. Mixing at Camarinal Sill in the Strait of Gibraltar. J. Geophys. Res. Oceans 99 (C5), 9847–9878. https://doi.org/10.1029/94JC00256.
Wunsch, C., Ferrari, R., 2004. Vertical mixing, energy, and the general circulation of the oceans. Annu. Rev. Fluid Mech. 36, 281–314. https://doi.org/10.1146/annurev.fluid.36.050802.122121.
Wunsch, S., Keller, K., 2013. Unstable modes of a sheared pycnocline above a stratified layer. Dyn. Atmos. Oceans 60, 1–27. https://doi.org/10.1016/j.dynatmoce.2012.12.001.
Zhu, K., Mao, K., Chen, X., Wang, J., Wu, H., 2021. A case study of the thermohaline fine-scale structure of the Sub-Artic Front. Atmos. Ocean 59 (3), 178–189. https://doi.org/10.1080/07055900.2021.1955328.
Zillman, J., 1972. A study of Some Aspects of the Radiation and Heat Budgets of the Southern Hemisphere Oceans. Australian Government Publishing Service, Meteorological study n, p. 26.